UNIVERSITY OF CALIFORNIA,
IRVINE

Numerical Simulation of Photoinduced Force Microscopy

THESIS

submitted in partial satisfaction of the requirements
for the degree of

MASTER OF SCIENCE
in Electrical and Computer Engineering

by

Mohammad Almajhadi

Thesis Committee:
Professor H. Kumar Wickramasinghe

Associate Professor Ozdal Boyraz

Associate Professor Eric Potma

2016

DEDICATION

To my parents

TABLE OF CONTENTS

LIST OF FIGURES

ACKNOWLEDGMENTS

My deepest gratitude to my committee chair, Professor H. Kumar Wickramasinghe. It is an honor to be one of his group member. He continually supervises and guides me to the right path. Without his guidance and persistent help this thesis would not have been possible.

I would like to thank my committee members Associate Professor Eric Potma and Associate Professor Ozdal Boyraz for reviewing my thesis and for their advises and comments. Furthermore, special thanks for Associate Professor Filippo Capolino who has reconsidered my application papers and helped giving me the chance to be part of University of California-Irvine.

ABSTRACT OF THE THESIS

Numerical Simulation of Photoinduced Force Microscopy

By

Mohammad Almajhadi

Master of Science in Electrical and Computer Engineering

University of California, Irvine, 2016

Professor H. Kumar Wickramasinghe, Chair

In this thesis we introduce a method of imaging: photoinduced force microscopy (PiFM). In this method, the images are accomplished by detecting tip-sample force at the near field which is optically excited. The origin of this force is related to the dipole momentum of the tip and its image in the sample. The dipole momentum strength is function of the polarizability of the sample under test; the polarizability is a wavelength dependent. Therefore, driving sample at resonance will give higher force than off resonance. This polarizability contains the spectroscopic information about the sample. By tuning the excited laser over broad range of frequency spectra, sample can by identified by comparing the resulting force measurement to a well-known absorption curve. PiFM Spatial resolution is well below 10nm and it is limited only by the tip geometry. This is because the field is spatially confined and the gradient of tip-sample force is proportional to z^{-4} where z is the distance away from the tip. Finite Element Method (FEM) is utilized to calculate the force gradient, and the tip-sample force.

The probe is attached to the end of a cantilever vibrating at one or two mechanical frequencies. Simultaneously, topographic and optical imaging process can be done by detecting them at different mechanical frequencies. In fact, the force will shift the mechanical frequencies, and this shift will be detected through quad-photodetector and the extracted signal will be translated into an image.

CHAPTER1: Introduction to Atomic Force Microscopy

1.1 Historical overview

Curiosity derives scientists for discovery, and scientific observations what make them sustain till they achieve great discoveries which elevate human's cognition and perception to a higher level, enhancing their ability to solve dilemma, which usually open new disciplines for next generations to elaborate. Seeing small features was a dilemma which was surmounted by inventing microscope; microscope is a device that allows us to see small features. In this introduction, we will briefly trace the progress of microscope from seeing biological cells to the atomic resolution.

Optical microscope has been developed steadily since Antoni Van Leeuwenhoek (1632-1723) who has constructed the simple microscope until the invention of the compound microscope. Biological cells were stained to visualize their structure through compound microscope. In 1935, phase contrast imaging was invented by Fritz Zernike. Because of this invention living cells can be observed without staining. In 1951, further development was done by Young and Roberts [1] who built the very first scanning optical microscope. For detailed history about scanning microscopy one can refers to the excellent review by H.K. Wickramasinghe [2]. The aforementioned microscopes are not skillful enough to capture features in atomic scale. Therefore, a new generation of microscope that is capable of distinguishing minute features becomes necessity. This generation should overcome Abbe's criterion that limits microscope resolution to one half of the incident wavelength, it should be gentle to avoid damaging the specimen by excessive energy or mechanical force and accurate to resolve features with atomic scale.

In 1982, a new era of microscope emerged by Binnig et al. when they successfully translated O'Keefe's principle to actual device taking the advantage of the ongoing development of manipulating objects with nanometer precision by Russell D. They called the device Scanning Tunneling Microscopy (STM) [3]. STM utilizes probe tip with one atom at its end. The probe and the sample are conductors. As the tip approaches the sample surface, tip-sample electron clouds interfere creating channel for electrons to tunnel once a voltage is applied to the tip. These tunneling electrons increases or decreases during scanning as the tip passes over bumps or holes. Current fluctuation which corresponds to the specimen surface will be measured and translated to a 2D image. STM is able to image single atoms, and, obviously, surmounts Abbe's criterion by far. The successful story of STM furnished the ground for the advent of new family of microscopes: scanning probe microscopes (SPM) [4]. Atomic force microscopy (AFM) was among the first arrivals. In fact, it was introduced in 1985 by Binnig, Calvin F. Quate, and Christoph Gerber. In the following section, the working principle of AFM will be illustrated.

1.2 Principle of operation

In this section we will provide an introduction of AFM in terms of working principle. Then we will elaborate to introduce the main instrument of AFM. Finally, three main modes of operation will be discussed: contact mode, non-contact mode, and tapping mode.

AFM, essentially, is a force senor. It has the ability to precisely measure small forces (10^{-15} N) limited only by the thermal fluctuation. In particular, the tip of the cantilever interacts with the sample. This interaction causes the cantilever to deflect (contact mode), or causes a shift in the cantilever resonance frequency (non-contact mode). The question one may

ask is why measuring tip-sample force is useful. It turns out that as the tip scans the sample, it follows the surface corrugation of the sample. Based on the recorded forces one can extract topographic image of a sample; AFM is capable of creating 3D images where these 3D images give information related to the surface of the sample but not the inner structure. For higher resolution images, AFM tip curvature radius should be as small as possible. AFM can perform well with conductors and insulators, and this is what makes AFM superior over STM. In addition, no specific sample preparation is required before scanning process.

AFM microscope consists of scanner which is nothing but a 3D positioning system. This part is responsible of adjusting the relative tip-sample distance according to a feedback system i.e. detected deflection is fed back to the scanner and the later adjusts the relative tip-sample distance. Then, these changes in the scanner position are translated to topographic image. Sample holder is an important part of AFM; it should be as stable as possible. In addition, AFM microscope includes cantilever beam with tip at its rear. AFM tip is made from silicon or silicon nitride and the cantilever is made from the same material. It is of concern to design a tip-holding structure that endures carrying the tip at the very end of it, and provides the flexibility to deflect. The tip should be fabricated so that its radius of curvature is in atomic scale. Finally, detection system must be installed, for the sensed information becomes recognizable.

To detect the deflection of the cantilever a light beam incidents on the very end of the cantilever, and it is reflected to quadrant photodetector (figure 1). The vertical section of the photodetector shows heights and gaps (up and down motions). On the other hand, the

horizontal sections detect the literal deflections that are due to shear forces. The photodetector converts light to current which is amplified and sent to the control circuit. The scanner—through the control circuit— adjusts the position of the tip with respect to the sample (or vice versa) i.e. by utilizing a piezoelectric.

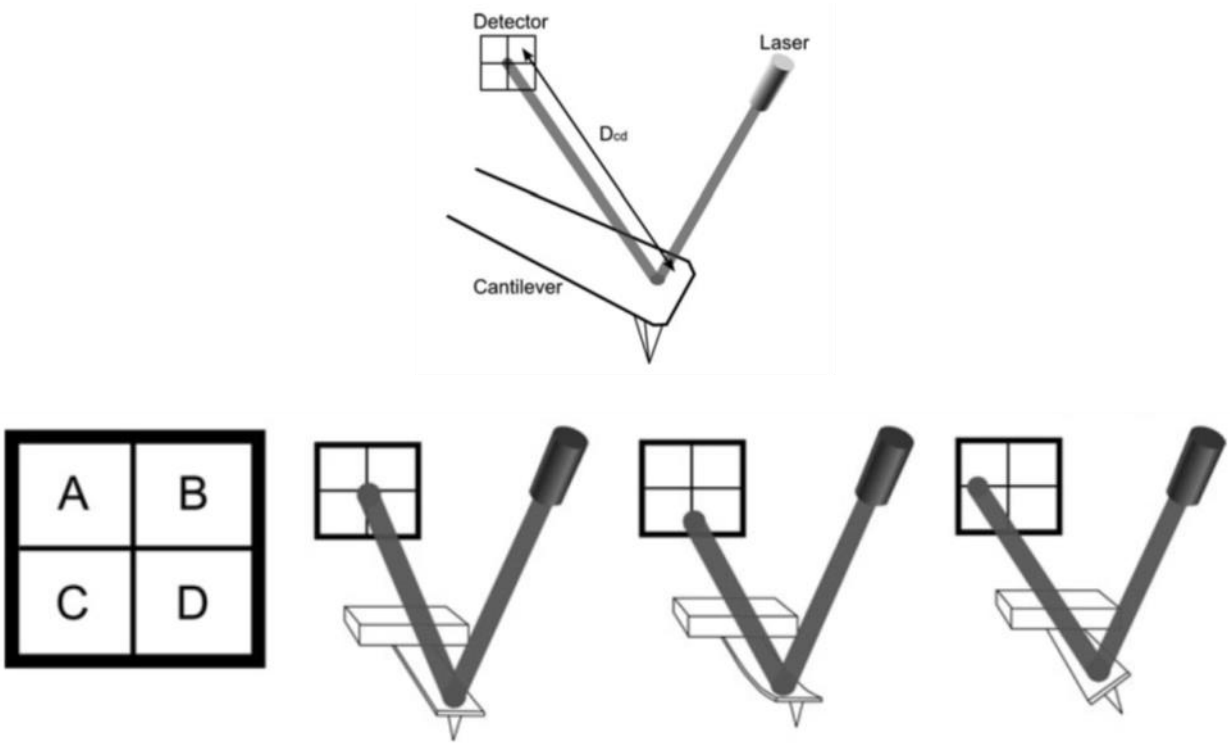

Figure 1: Detection method of cantilever motion. The box is the quad photodetector. Adopted from [5].

AFM operations modes are generally three: contact, non-contact, and tapping modes. These modes are interacting with the sample morphology. This interaction manifests itself as shift in frequency or deflection in the cantilever. Utilizing different methods, one can probe different type of material properties. For example, by utilizing contact mode method, sample features can be probed since the tip is in a direct contact with the sample, where

the tip force needs to be maintained by feedback system to avoid damage or deformation of the sample caused by dragging forces. If atomic forces, electrical, or magnetic forces are of importance, the non-contact mode should be utilized. Thus, these modes are employed in different applications. The tip-sample force behavior can be understood by classifying it into attractive and repulsive forces. As the tip is approaching the sample, the tip-sample force is attractive van der Waals force. Once the electron clouds of the tip and the surface atoms see each other, a repulsive van der Waals force will dominate; van der Waals forces can be repulsive or attractive depending on the tip-sample distance. Therefore, in the contact mode the force is mainly repulsive while attractive force is dominant in the non-contact mode. The tapping mode utilizes the same principle of non-contact mode; the cantilever vibrates at natural frequency, and the information is taking by measuring the shift in the frequency. The difference is that in non-contact mode the tip never touches the sample, while in tapping mode tip touches the sample. Therefore, the tip is exposed to attractive and repulsive forces in one cycle. This method can be employed to image soft sample, which cannot be done by the contact mode.

1.3 Application

Applications of AFM are very diverse, and it is hard to cover all of them in this introduction. Instead, three categories will be illustrated: applications in physical and material science, in nanotechnology, and in biology [5]

AFM gives the ability to measure surface roughness of a material because AFM shows 3D images with high contrast between the rough and smooth parts of a surface. Scanning electron microscopy (SEM) is employed, but it cannot resolve surface roughness with 100Å

or below. Because AFM does not have this limitation, it becomes the first choice for such application. Generally, roughness affects material properties such as optical and adhesion to other materials; high resolution images of surfaces allows better understanding of roughness effect, and AFM capable of generating high resolution images. Atomic resolution images are not useful if the sample consists of deferent molecules that are not organized. Thus, very pure samples are a prerequisite, for atomic resolution images to be useful and interpretable. In fact, atomic resolution images are those that allows observer to distinguish atoms features individually [5], and this is achievable by scanning tunneling microscope STM only. AFM images does not discriminate individuals atoms but the average arrangement of atoms i.e. it shows atomic lattice resolution. This point is emphasized for clarity, but 'atomic resolution' will be used throughout the thesis and it means atomic lattice resolution. Another application that belongs to physical and material science category is friction measurement. Through lateral forces microscopy (LFM), which is an AFM mode of operation, tribology discipline can be studied. Friction properties of materials can be imaged, which leads to the characterization of heterogeneous materials. LFM is not the only technique for friction measurements. However, it allows friction measurements in nanoscale.

Applications in nanotechnology require a technique that is capable of measuring local properties of a material. To have access to local property, the technique should employ high resolution device. These two main features exist in the AFM technique. In addition, AFM illustrates information extracted from the sample in 3D. All these advantages make the AFM excellent method for nanotechnology and nanoscience application. The properties of a material are proportion to its size. Therefore, AFM has been utilized intensively for

measuring nanoparticles size with high precision. These nanoparticles can be conductive or nonconductive. In addition, manipulating nanoparticle or any nanostructures is possible by using AFM. For example, sample electrical properties can be examined by positioning the sample utilizing AFM tip between two electrodes currying current.

AFM Applications extend to the study of biological cells. It is of importance to study these cells in physiological-like conditions because biological cells alter their structure when dried. Finding a device that can operate normally under the physiological-like conditions is a challenge that has been overcome by the invention of AFM. Most of biological samples are probed in liquid, which consists, in most cases, of salt to achieve physiological-like conditions. Because cells are considered as soft samples, non-contact mode is utilized to avoid damaging the samples. Thus, AFM has two key advantages: its ability to work in liquid, non-destructive mode of operation. By combining these two advantages with high imaging resolution, biomolecule imaging using AFM has been widely investigated.

Readers who are interested in AFM applications are referred to [5]. For profound understanding in how AFM is utilized in biological applications, readers are referred to [6].

CHAPTER 2: Optically Dressed AFM

2.1 Scanning Near Field Optical Microscopy (SNOM)

2.1.1 Introduction

Classical optical microscopy is limited to Rayleigh criterion $0.61\lambda/NA$, where NA is the numerical aperture and λ is the wavelength. With this condition, the best resolution can be achieved is 0.2-0.5 micrometer in the optical frequency, which is not suitable for studying local properties of a sample, and by local we mean spots with molecular dimension. In 1928, Synge addressed this problem by proposing a scheme, which is then called scanning near-field optical microscopy (SNOM), that can beat diffraction limit. A subwavelength illuminated aperture acts as subwavelength light source which is placed in the near-field region to a transparent substrate. The image is not formed by diffraction-limited lens but by collecting the scattered light by sample; this scattered light carries information about fraction of the sample. This fraction size is determined by the size of the aperture [10]. Due to technology limitation, Synge's proposal is reborn after 4 decades by Ash and Nicholls [11]. They could achieve $\lambda/60$ spatial resolution in the microwave regime.

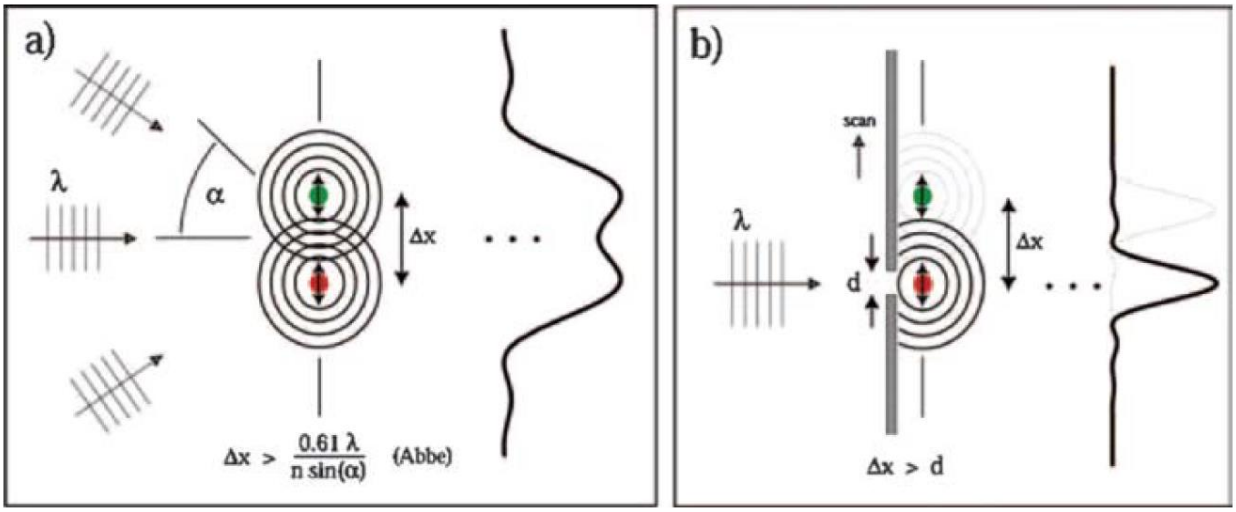

Figure 2: It shows the principle of Synge. (A) two molecules illuminated together; no possible contrast. (B) one gets illuminated by the help of the aperture; possible contrast. Adopted from [44].

Figure 2 illustrates the diffraction limit and Synge's principle. Assume we have a sample that consists of two molecules. If a plane wave is incident on the sample, then both molecules will get excited. The generated scattered field from both molecules will overlap so that no possible contrast can be detected (overlapped peaks). With the help of the aperture one molecules can be excited, and one pattern of scattered field can be generated and, therefore, detected. The aperture radius is much smaller than the incident wavelength; it's 100nm as Synge proposes, and the aperture-sample distance, to insure local excitement, is no greater than the radius of the aperture. The incident wave suffers from severe attenuation proportional to the aperture radius. In fact, the output radiation is an evanescent wave at nano-scale aperture. Because of this attenuation, the aperture-sample distance must be as small as possible for better performance. In other words, for better images, targeted sample should scatter adequate amount of radiation.

By the advent of the scanning probe microscopy (SPM) controlling aperture-sample distance within nanometer scale become possible. In addition, the opaque metal layer is

replaced by probe which guides light into the sample and scattered light from sample to the detector. After implementing Synge's proposal successfully, the next step is to shrink the size of the aperture to reach atomic resolution. Unfortunately, as aperture size decreases the transmitted light intensity becomes insufficient to be scattered by sample; it must be large enough for light to penetrate the aperture. This is true for light source probe or light collector probe as will be introduced in the next section. This put a limit to SNOM spatial resolution. Practically, aperture cannot be smaller than 50nm, where at this size the decay rate is proportional to the 10^5. The evanescent loss at the aperture can be overcome by increasing the intensity input, but it turns out that increasing the intensity cause excessive heat that could damage the probe. In the next section the principle of SNOM will be introduced and its limitation will be highlighted.

2.1.2 Principle of Operation

Figure 2 illustrates general set up of the SNOM. It consists of three main units: illumination light unit, light collection unit and finally detection unit. In this set up, the laser light is lunched and its polarization is control before coupling it to the fiber. The light is coupled and guided by probe having at its apex an aperture small enough to locally illuminate the sample. The probe is glued into a tuning fork that is attached to the piezoelectric responsible for driving the fork mechanically, therefore, driving the probe to oscillate laterally into its near resonance with vibrating amplitude in the range of 1nm to 5nm. Van der Waals forces interact with the probe and shifts the resonance peak.

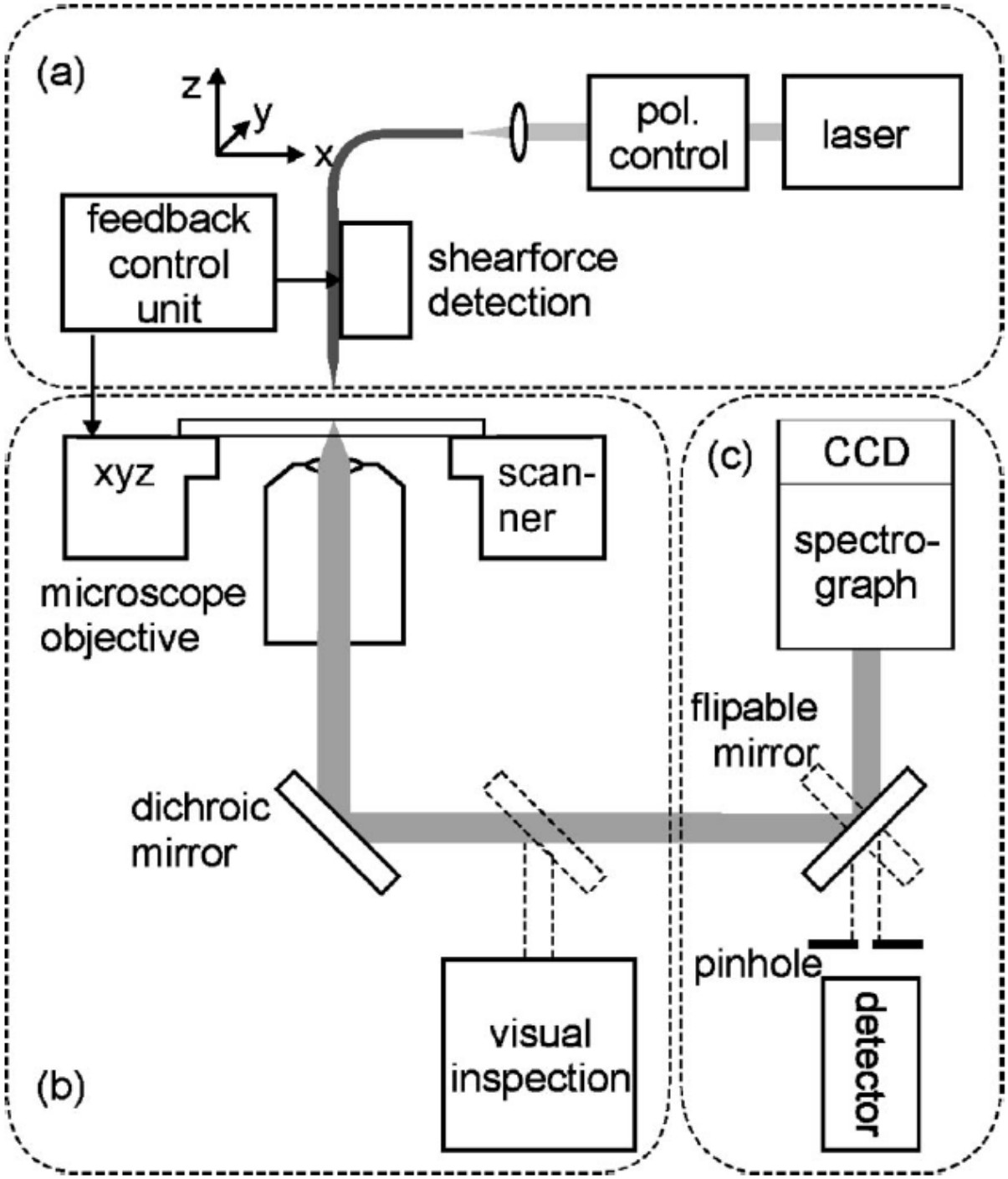

Figure 3: (a) Illumination unit. (b) Collecting and distribution unit. (c) Detection module. Adopted from [19].

Therefore, sample corrugation will change the resonance as the probe raster-scan the sample i.e. it causes phase shift. In addition, the oscillation amplitude is changing while approaching the sample, but practically phase signal is used due its fast response to the change. In fact, the feedback is either pure phase feedback [12], or phase and amplitude feedback [13][14][15], but not pure amplitude feedback due its slow response. To keep the probe-sample distance fixed, AFM feedback unit, which is called shear force feedback [16][17], is installed to adjust the height based on the shift in the resonance. The setup provide control in the lateral axis i.e. to move the probe into a specific area.

Exciting light needs to be collected after interacting with the sample. For effective collection, high NA microscope objective must be used. Practically, an oil immersion aperture is used specially if the substrate is flat because light may undergo total internal reflection and never go to the detector. This light is called forbidden light. Obviously, collecting this forbidden light will give better images [18]. Once light is collected, it is redirected through dichroic mirror. Finally, it is sent to the detector after filtering the unwanted spectral component from the light through the pin hole.

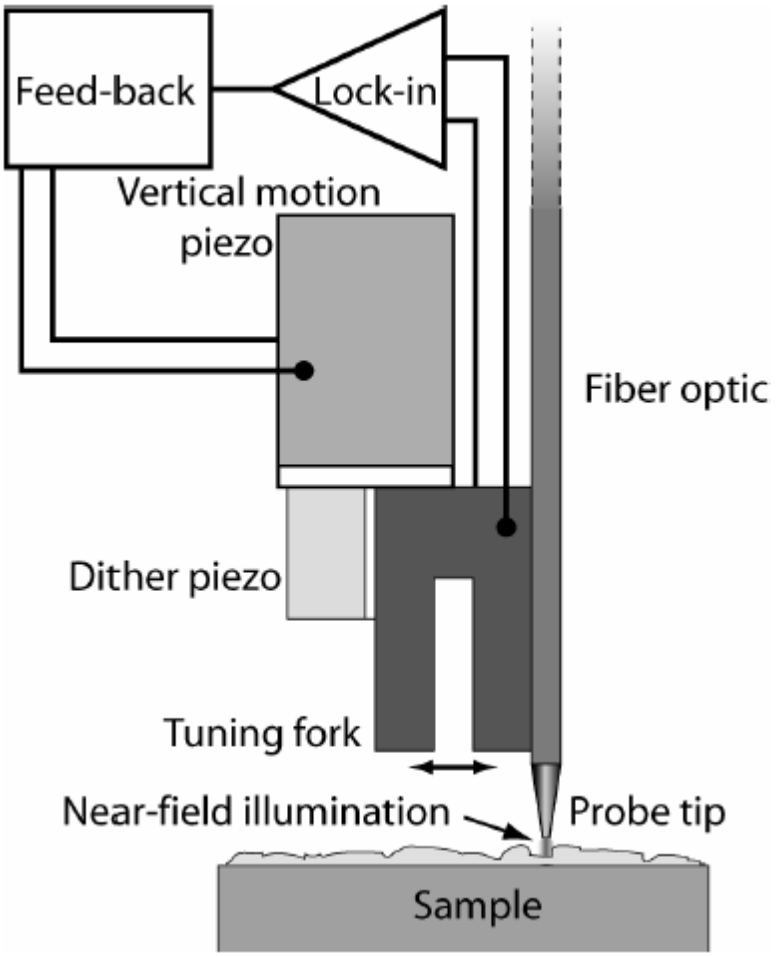

Figure 4: Set up configuration for controlling the probe-sample distance. Adopted from [45].

There are two main steps to fabricate near-field optical probe. First, transparent tapper probe with sharp apex is created. Second, coating probe wall by metal i.e. aluminum so that the probe become opaque. The end apex of the probe is not covered by the coating to create the aperture. These two steps can be done either by heating and pulling method or through chemical etching [19].

The fiber is locally heated i.e. using CO_2 laser, and at specific temperature and certain time the fiber is pulled. Timing, temperature, and heated spot size must be taken into account

for better probe design [20] [21]. The probe is coated through evaporation, and to increase the evaporation layer quality, the fiber walls should be as smooth as possible; this can be achieved using heating method. In addition, apex will be flat which is suitable for emitting or collecting light, but it is not suitable for scanning rough surfaces because the tip cannot follow the topography of the surface. In general, light transmission through the apex is low due to the small cone angle that is hardly increased using this method. Figure 5 (left) shows the resulting probe using heating and pulling method.

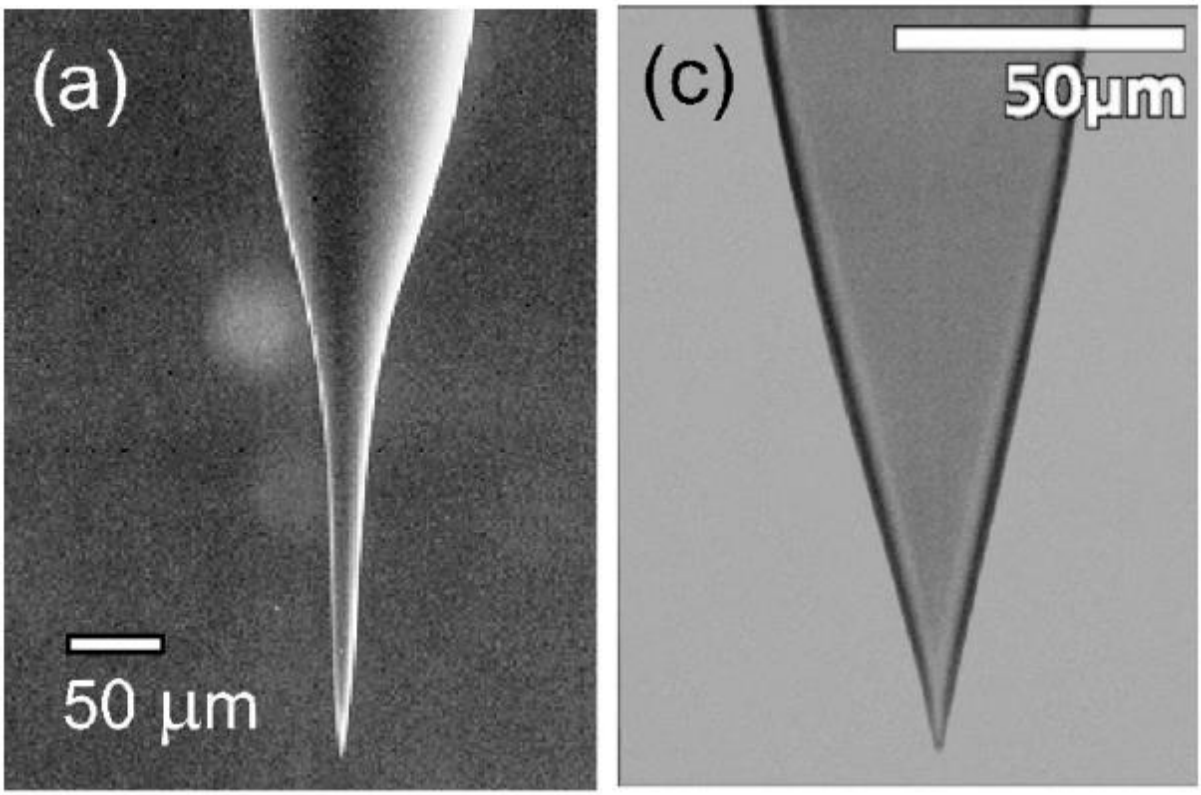

Figure 5: Probe design using heating and pulling method (left), and chemical etching (right). Adopted from [19]

In 1984, Turner proposed a technique that would help designing probe using chemical etching, and it was first implemented by P. Hoffmann et. al. in 1995 [22][23]. The Idea is to immerse the cleaved fiber into hydrofluoric (HF) acid covered by protection layer; this

protection layer can be organic solvent. The aqueous etching solution will chemically attack the immersed part of the fiber (see figure 6). The protection layer will gradually cover the attacked part to create tetrahedral shape with large cone angle. This cone angle responsible for high transmission coefficient can be controlled by changing the protection layer composition and by the original fiber diameter [23]. The only disadvantage of using chemical etching is that it creates irregularities in the formed probe. This leads, after aluminum coating, into light leakage through the tip walls. This problem, however, has been solved by P. Lambelet *et al*, where, in there experiment, etching caused by diffusion process through the fiber jacket which is not included in Turner proposal [24].

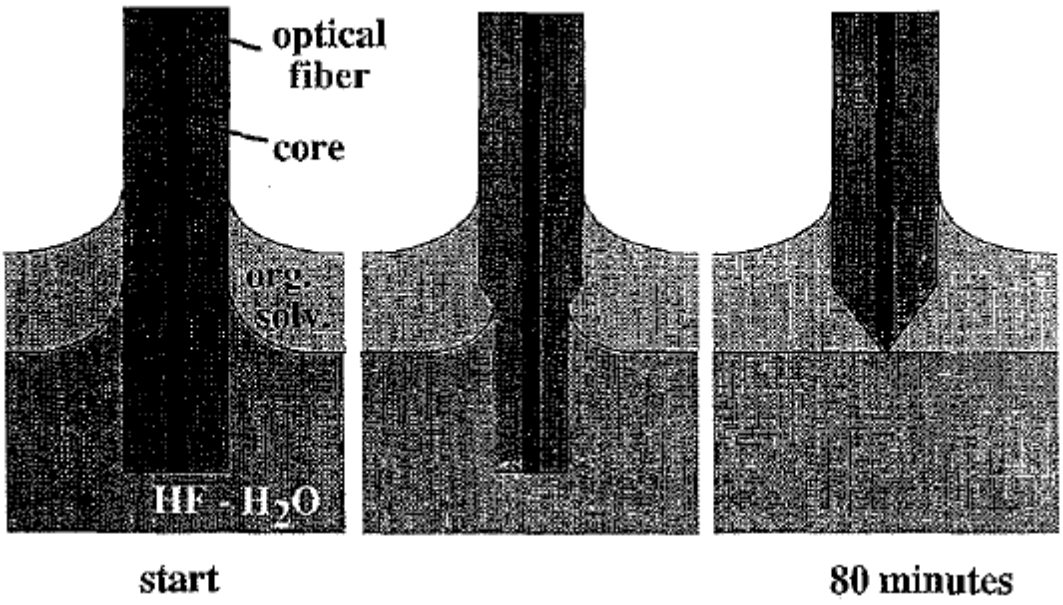

Figure 6: Schematic geometries of the liquid layer protection etching. Adopted from [23]

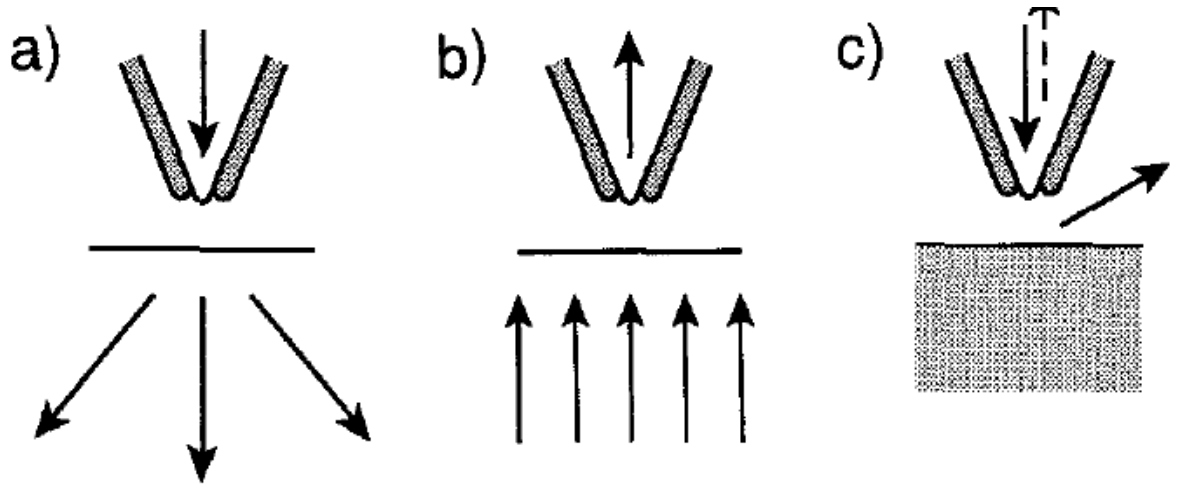

Figure 7: Different methods of doing SNOM. Adopted from [25]

Figure 7 illustrates several modes of operation of doing SNOM. Fig.7(a) the tip is used as a light source to illuminate locally the sample. Then the light is collected once it interacts with the sample through light collection unit, filtered through pin hole to remove unwanted spectra, and detected by the photodetector. This method is important for fluorescence application. The tip can be a light collecting. The sample is illuminated from the far-field, and light that undergoes total internal reflection causes evanescent waves at the surface which interacts with the tip and propagates through the aperture to be detected by the photodetector. This mode suffers from signal obscuring caused by field scattering and interference Fig.7(b). For opaque sample, the operation mode shown in Fig.7(c) is utilized. Dielectric probe illuminates the opaque sample and the reflecting light is collected by the probe itself. If compared to the radiation background, the collected signal intensity is weak and this causes a problem at the detection unit [25]. An alternative way of doing SNOM is invented by H. K. Wickramasinghe and C. C. Williams in 1990 [26]. The tip is utilized as scatterer to the evanescent field generated near the surface. This method will be introduced in detailed in section 2.2.

2.1.3 Applications

Aperture SNOM extracted the images through contrast difference; this contrast can be phase or amplitude contrast, and depending on the type of contrast the applications can vary. For example, Aperture SNOM with phase contrast can be employed to image dielectric grating. The difference in the dielectric cause difference in the optical path which is translated into phase difference. In this application, probe-sample distance is important for high resolution image; it must be in the order of few nanometers for better images [27]. For amplitude contrast application, SNOM can be good imaging technique for metal island film; by measuring the relative light intensity while scanning, metal island can be imaged with resolution in the order of 50nm [27]. Another application for SNOM is fluorescence imaging. SNOM capable to image single molecule fluorescence, which was accomplish by Betzig and Chichester in 1993 [28]. It opens opportunities to study the dynamic behavior of the single molecule. In addition, SNOM can operate under ambient condition or biological cells native environment which is advantageous for studying living cells. SNOM is well suited for biomedical applications. For example, Photosynthetic Systems can be imaged with high resolution. Studying the distribution of photosynthetic protein in membranes has been reported [29] [30] [31]. Furthermore, chromosome mapping related applications have been implemented using SNOM and reported [32] [33] [34]. For more details about SNOM applications, the readers are referred to the excellent review done by Robert C. Dunn [35].

2.2 Scattering-Type Scanning Near Field Optical Microscopy SNOM

2.2.1 Introduction:

Despite the advantages of aperture NSOM for studying and extracting spectroscopic information through light-matter interaction, it has limitations that limits its applicability in nanoscience applications. For example, the transmission coefficient when using the optical probe as light source suffers from severe degradation, and compensating this loss by increasing the input power need not to be considered if it leads to probe damage by excessive heating caused by metallic absorption. Other limitation is related to the difficulty to produce smooth coated-metal walls. In addition, probe apex is flat, and this is not suitable for extracting surface topography. In other words, the probe cannot follow the corrugation of the sample accurately, therefore, limiting the spatial resolution. Thus, a better technique that overcomes these obstacles is necessary. In 1990, H. K. Wickramasinghe and C. C. Williams introduce for the first time scattering type NSOM [26]; it is called scattering-type SNOM (sSNOM) or apertureless SNOM (aSNOM).

Figure 8 illustrates the principle of sSNOM (left) and its realization as proposed by [26]. In sSNOM the probe acts as a scatterer object. It converts the evanescent wave into propagating wave which will be detected at the far field by photodetector. sSNOM, obviously, overcomes the SNOM limitations. For example, while SNOM is limited to certain wavelength region, where this region is related to the transmission coefficient, sSNOM application can be extended from optics to infrared regime. The spatial resolution, in sSNOM, is limited by the tip apex radius which is limited by fabrication technology available. On the other hand, SNOM aperture radius is governed by the transmission

coefficient which limits its spatial resolution. Fabricating sSNOM probes are much easier than those in SNOM because they will not be used as illuminating sources but rather scatterers.

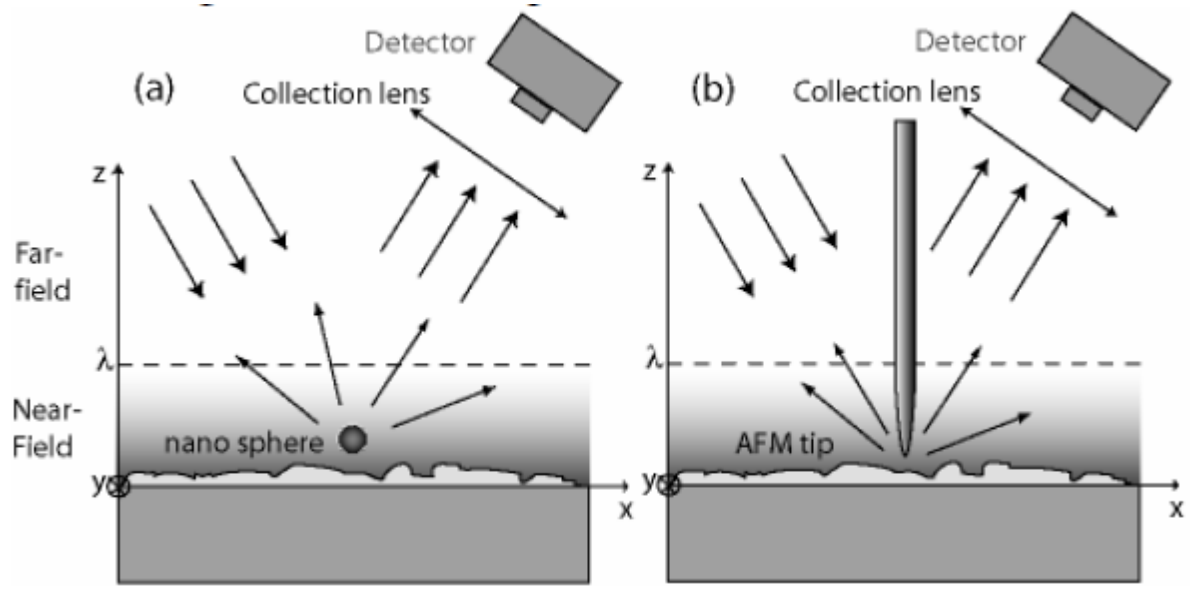

Figure 8: Scattering type NSOM principle of operation. Adopted from [45].

2.2.2 Principle of operation

The incident light is focused into the scatterer which is in this case an AFM tip or STM tip. The tip approaches the sample, through AFM control unit, to locally scatter the evanescent field. Once the tip approaches the sample surface the tip enhances the field into orders of magnitudes depending on excitation wavelength, coating material, tip-sample distance, and tip geometry. That means that the tip is not only an antenna but also a local light source. The enhancement originated from tip-sample optical coupling at the near-field distances, and electronic transition (chemical effect). This enhancement can be further increased when plasmon effect is involved by employing noble metal as a coating material. The

enhancement is very confined near the tip apex, and this helps increase the spatial resolution of the sSNOM.

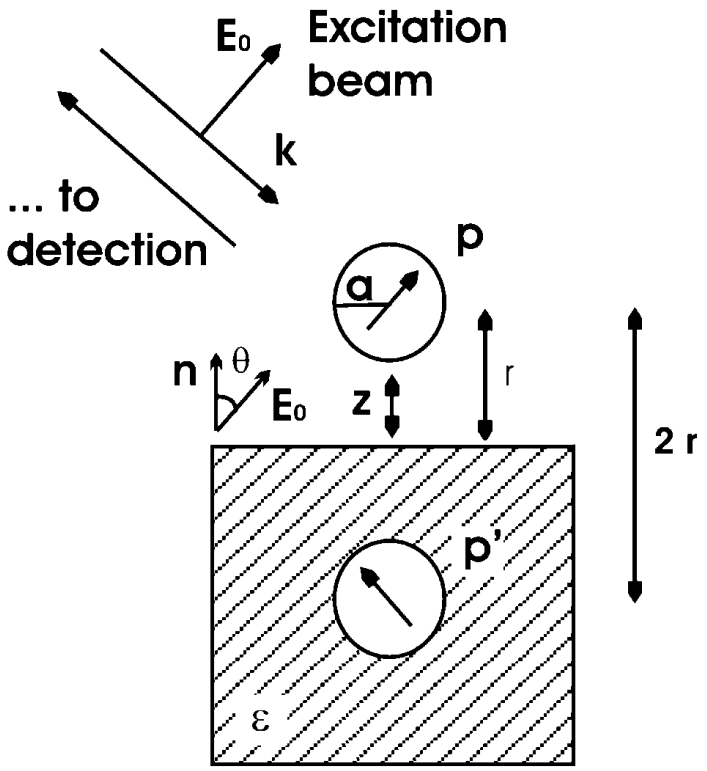

Figure 9: Quasi-electrostatic approximation (dipole approximation). Adopted from [40]

To understand the physics involved in the enhanced region, the dipole approximation will be explained. The tip is considered as a polarized sphere with dipole moment; this dipole creates its image on the substrate. Therefore, the field in any dipole is a superposition of the incident field and the field induced by the other dipole. As illustrated in figure 9, center to center distance between the dipoles is 2r, where r is the distance from dipole center to the substrate surface. The polarizability of the sphere with radius a is $\alpha_t = \frac{a^3(\varepsilon_t - 1)}{\varepsilon_t + 2}$ [36], where the subscription t denotes the tip polarizability, and ε_t is the dielectric function of the tip. Any polarizable object subject to an electric field will generate dipole moment **P** (bold indicates vector quantity), where it is related to the electric field through the

polarizability α_t; this dipole momentum is also affected by the field incident from the image dipole. The total dipole momentum generated at the tip is:

$$\boldsymbol{P} = \alpha_t\big(\boldsymbol{E} + \boldsymbol{E}(\tilde{r})\big) \qquad 2.2.2.1$$

The image dipole field calculated at the location of the tip dipole is

$$\boldsymbol{E}(\tilde{r}) = \frac{3\big((\tilde{n}.\boldsymbol{P'})\tilde{n} - \boldsymbol{P'}\big)}{8r^3} \qquad 2.2.2.2$$

$\tilde{n}$ is the surface normal and **P**' is the image dipole momentum. The field of image dipole is inversely proportional to the distance cube r^{-3}; this means the further the tip the less the image field to contribute in the field enhancement. According to [37], the optical coupling between the sample and the tip can be found by calculating the effective polarizability α_{eff}. The effect of the image dipole field is embedded into α_{eff}.

$$\alpha_{eff} = \alpha_t(1 + \beta cos\theta)E_{inh} \qquad 2.2.2.3$$

$$\beta = \frac{\varepsilon - 1}{\varepsilon + 1} \qquad 2.2.2.4$$

$$E_{inh} = \frac{1}{1 - \left(\frac{\varepsilon_t - 1}{\varepsilon_t + 2}\right)(\beta)\left(\frac{1 + \cos^2\theta}{8}\right)\left(\frac{a}{a+z}\right)^3} \qquad 2.2.2.4$$

E_{inh}, ε, and z are the electric field enhancement located in the tip-sample gap, the dielectric function of the sample, and the gap distance respectively. The angle θ is the angle between the light polarization i.e. electric field (E) orientation, and the surface normal. To increase the enhancement, the electric field polarization should coincide with the surface normal, and the tip-sample gap should be as small as possible. Note that when θ = 0, the two dipoles fields are constructive fields while they are cancelling each other in the case when θ = π/2.

Experimentally, however, the dipoles fields may not cancel each other; these analyses are an approximation. It gives us an idea about the behavior of the tip-sample optical coupling.

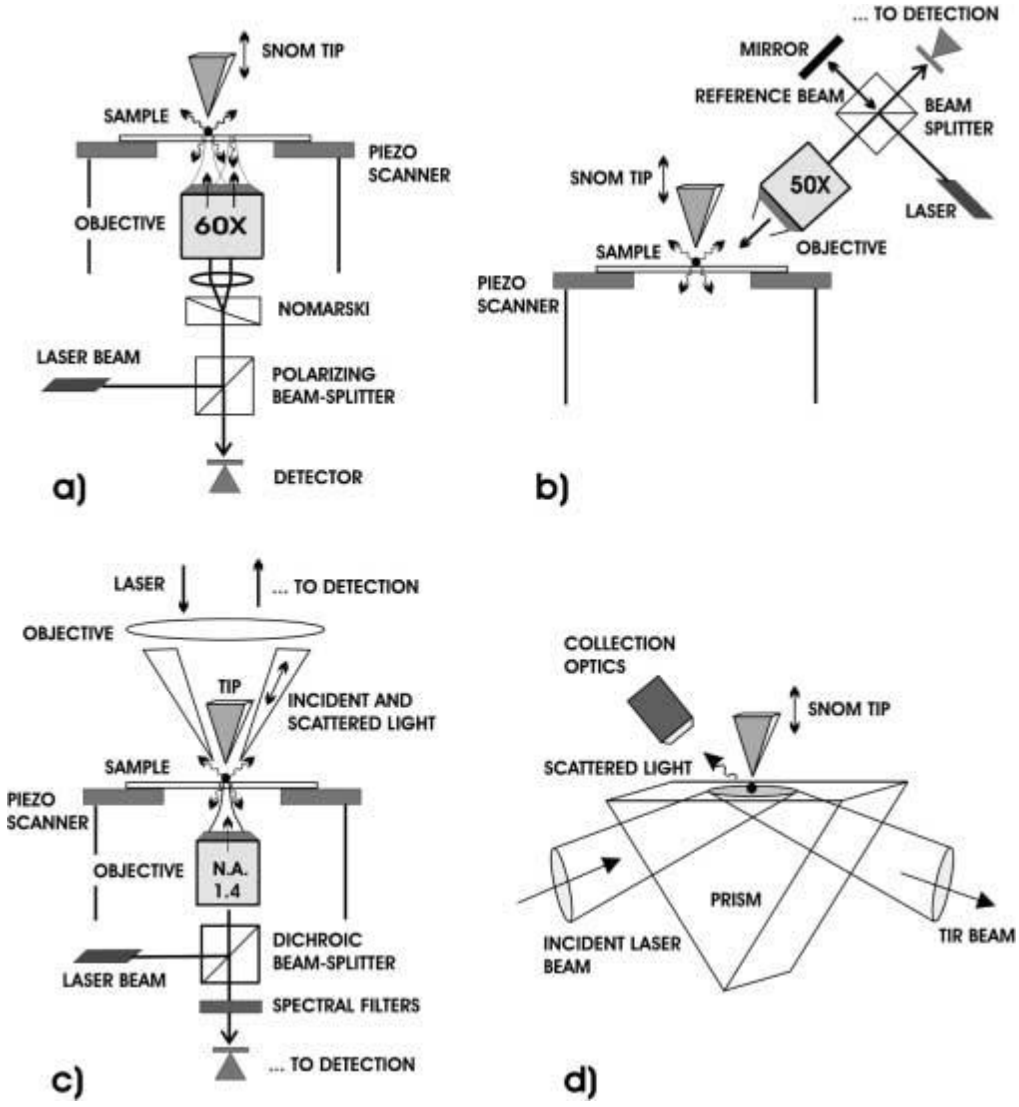

Figure 10: Setup configurations for sSNOM. (a) Interferometric transmission mode and (b) reflection mode. (c) Non-interferometric mode. (d) Setup for evanescent wave. Adopted from [40].

AFM non-contact mode is the main mode used for sSNOM setup. The tip is located at the end of cantilever, and the cantilever is driven at one of it mechanical oscillation frequency. The oscillation amplitude is in the order of few nanometers, and the oscillation direction is parallel to the surface normal. The oscillation amplitude is detected optically or through

piezoelectric, but the most common method is optical detection. As illustrated in figure 11, light beam is incident on the back of the cantilever; approximately, at the end of the cantilever where the tip is located. The quad-photodetector detect the reflected signal. This signal is use to detect the oscillation amplitude. The tip is metalized through coating to enhance the field in the gap. As a consequence, the scattered field is enhanced. The amplitude of the oscillation is kept fixed through AFM unit feedback that utilize a piezoelectric which works out of plane from the sample surface. Hence, the sample topography can be extracted simultaneously with optical information.

Figure 10 shows different setup that sSNOM can operate with. Interferometric mode is used to study, mainly, the elastic-scattering properties of the sample i.e. refractive index measurement. In other words, the detected signal is the scattered light. For inelastic measurement, non-interferometric mode is utilized. In this mode the scattered intensity is the measured quantity. This method is suitable for Raman, photoluminescence, and second-harmonic generation applications. These two modes differ from each other based on light illumination and light collection implementation.

Interferometric mode is first illustrated by Wickramasinghe [38], which is shown in figure 10(a). In this mode, a light beam is incident on a beam splitter, and is sent to the objective that focus the beam into two diffraction limited spots. The tip approaches one of these spot. The scattered field then is a combination of scattered field due to the tip (tip-scattered field) and due to the sample (back-scattered field). These two components are filtered and send back to the photodetector which detect the amplitude and the phase shift between the

tip-scattered field and the back-scattered field; this phase shift is responsible of the contrast.

The non-interferometric mode is used to measure the intensity of the scattered light. the illumination will be focused using long distance lens and this lens will act as light source and light collector. Alternatively, the illumination can be done using bottom illumination where the scattered light pass through filter and collected by, favorably, very sensitive photodetector (see figure 10(c)). The last mode of operation is the evanescent mode. A sample is set on a prism, and light beam with angle below the critical angle is incident on the prism surface. The light will undergo total internal reflection which will generate evanescent wave. The metallic probe will perturb locally the evanescent wave and the scattered light will be collected through a collection optics unit.

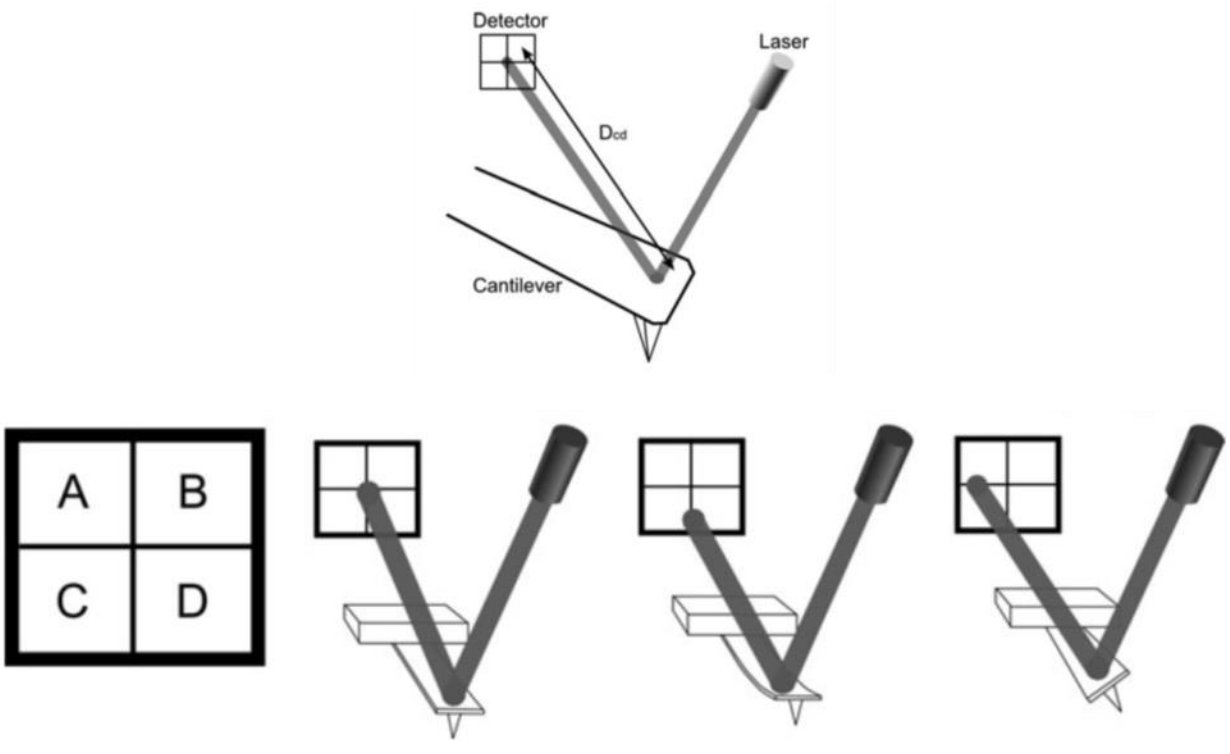

Figure 11: Figure 1 is repeated for convenience.

2.2.3 Applications

As mentioned above, sSNOM in interferometric mode is mainly employed to measure the elastic scattering light from a sample. Thus, elastic scattering imaging is an important application. In other words, sSNOM optically discriminates sample composition through elastic scattering light. For example, Fisher U. C. et al imaged what so called “Fischer patterns” sample which are made of metal shaped in triangular structure, using the principle of elastic scattering [39]. This experiment becomes standard test for sSNOM resolution. Another important application for sSNOM is Raman spectroscopy. The combination of the near-field optics with Raman (near-field Raman) allows dynamic and electronic study with nano-spatial resolution. Single molecule structure and electronic information can be extracted with the help of a sharp metallic tip. Raman signal is extremely small and it is not detectable for single molecule, but surface plasmon resonance and antenna effect can enhance the field by several order of magnitude making Raman signal detectable in nanoscale allowing single molecule resolution. This means that the Si tips are not used in near-field Raman imaging application because Si tips have weak field-enhancement. Because Raman technique is a non-invasive, it has been utilized in many applications in nanotechnology and biotechnology [40]. For example, Achim Hartschuh et al. used near-field Raman technique to image single isolated single-walled nanotube with spatial resolution of 25nm using silver-coated tip with tip radius of 10-15nm with excitation wavelength of 633nm [41]. In general, the enhancement is a function of geometry, coating material, tip apex radius, and tip-sample distance. Raman signal at nanoscale is detectable when the tip-sample distance is smaller than the tip apex radius because the largest field enhancement manifests at tip-sample distance much smaller than

the tip apex radius. Another example, Norikiko Hayazawa el at. imaged nanocrystallized Rhodamine6G and Crystal Violet molecules using near-field Raman technique [42].

2.3 Photoinduced Force Microscopy

2.3.1 Introduction:

In 2010, Rajapaksa et al demonstrates for the first time a technique, which is then called photo-induced force microscopy (PiFM), that images molecular resonance by sensing the mechanical force due to the interaction between sample dipole which is optically excited and its image in a polarizable tip; as a result, maps of local optical force is produced. In this methods, the atomic resolution provided by a sharp AFM tip is employed to extract local spectroscopic information provided by optical excitation. Unlike SNOM and sSNOM, the tip in PiFM senses the evanescent waves directly. In other words, PiFM is near-field detection technique. This force is related to the polarizability of the tip and the sample. Therefore, chemical information can be extracted using this technique. Because probed force is spatially confined in nanoscale, PiFM is capable of providing spectroscopic information with high spatial resolution well below 10nm.

The detected force is proportional to the tip-sample polarizability and the gradient of the field. The polarization can be complex, which leads to gradient force and scattering force. Gradient force is related to the inhomogeneity, while scattering force is related to momentum transfer to a polarizable object by light fields. To understand optical force on a tip approaching sample, the principle of dipole-dipole interaction between tip and sample can be used. In this principle, the tip and sample are approximated to be dipoles. The optical force is, then, proportional to the strength of these dipoles. In other words, driving sample at resonance and off resonance will show high contrast in spectroscopic imaging. Both dipoles are assumed to be point dipoles; this assumption allows having analytical expression which help enhances our understanding in the nature of forces at play. The total

force (F_{tot}) exerted on the tip must include van der Waal's forces, meniscus forces, chemical and Casimir forces (F_{int}).

2.3.2 Principle of operation

Spectroscopic information depends on optical excitation. Optically excited molecule or structure can be scanned using different methods as mentioned previously. What makes PiFM unique is that it is not limited by far field detection sensitivity; it is, only, limited by the tip geometry because it directly senses the local optical forces between the tip and sample. When the tip approaches the irradiated sample by light, tip-sample field is enhanced and the optical force is enhanced, which depends on the spectroscopic property of the sample. The principle of dipole-dipole interaction between tip and sample is illustrated in figure 12(b).

Every dipole consists of magnetic and electric momentum. Some material exhibit high electric momentum such as metal, while dense dielectric and metal clusters can exhibit magnetic momentum. Depending on experimental set up one can ignore the momentum that is not dominant. In general, the optical force can be divided into three main components: time-averaged force due to electrical dipole, time-averaged force due to magnetic dipole, and interaction force between electrical and magnetic dipoles. It is assumed that the electric and magnetic momentum are spatially non-varying. However, the total force (F_{tot}) exerted in the tip must include van der Waal's forces, meniscus forces, chemical and Casimir forces (F_{int}).

$$F_{tot} = F_{opt} + F_{int} \qquad 2.3.2.1$$

For more physical insight into the nature of the optical forces analytical approach is needed. This approach relies on the assumption that the tip and sample can be assumed to be point dipole. Field across point dipole is constant, which simplifies the analysis by far. Optical forces are function of the polarizabilities of the tip and sample. The polarizability ($\alpha = \alpha_r + j\alpha_i$) consists of dispersive component (α_r) and dissipative component (α_i). Based on the polarizability component optical forces can be decomposed into scattering force caused by the imaginary part and gradient force caused by the dispersive component.

$$< F > = < \frac{\alpha_r}{2} \sum_i Re\{E_i^* \nabla E_i\} > + < \frac{\alpha_i}{2} \sum_i Im\{E_i^* \nabla E_i\} > \qquad 2.3.2.2$$

Based on the geometrical set up optical forces can be classified into optical tweezer force, When the tip is irradiated with no substrate, image dipole force, when tip is irradiated above semi-infinite substrate, and optical binding force, when tip is mediated above polarizable object (see figure 12). The cantilever tip is sensitive to the z-component of the optical force. Thus, other components will be ignored for simplicity.

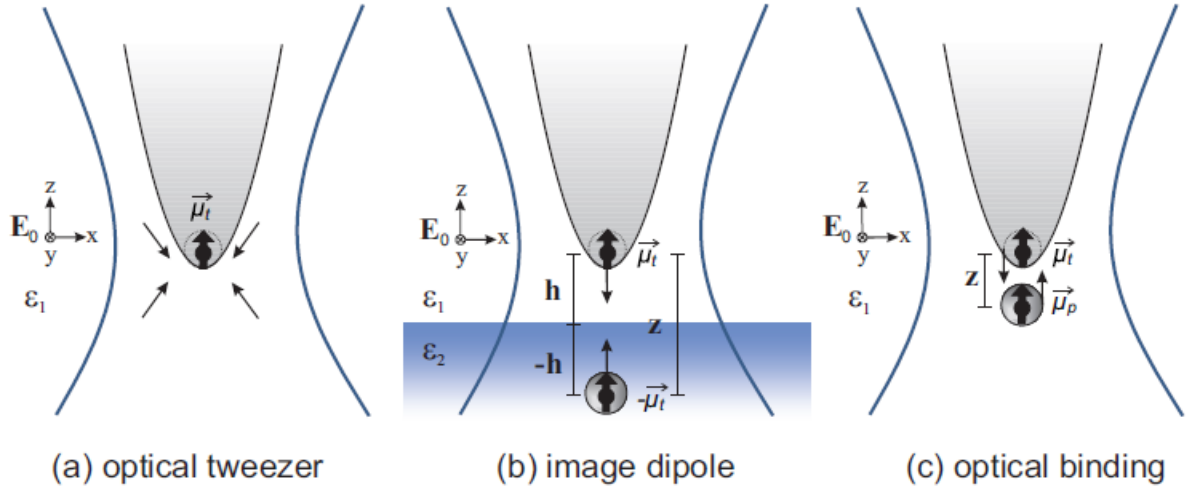

Figure 12: The three different types of forces are graphically illustrated. Adopted from [59].

Image dipole approximation takes into account the tip-sample mutual coupling due to optical excitation. The tip-substrate geometry will be a dipole with dipole moment consists of z component only, and its image on the substrate that consists of z component as well. The dipole momentum is proportional to the incident field through dipole polarizability. For detailed force analysis please refer to [59] and [60]. However, the final results will be mentioned and discussed. The scattering force $< F_{sc} >$ and the gradient force $< F_g >$ can be written as:

$$< F_{sc} > = -\frac{3\alpha_{it_z}\alpha_{it'_z}}{2\varepsilon_o \pi z^4}|E_{oz}|^2\tilde{z} + \frac{k}{2}\alpha_{it_z}|E_{ox}|^2\tilde{z} \qquad 2.3.2.3$$

$$< F_g > = -\frac{3\alpha_{rt_z}\alpha_{rt'_z}}{2\varepsilon_o \pi z^4}|E_{oz}|^2\tilde{z} \qquad 2.3.2.4$$

$\alpha_{it_z}, \alpha_{it'_z}, \alpha_{rt_z}, \alpha_{rt'_z}, E_{oz}, E_{ox}, and\ k$ are imaginary component of the tip polarizability, imaginary component of the image polarizability, real component of the tip polarizability, real component of the image polarizability, z component of the incident field, x component of the incident field, and the wavenumber respectively. Note that the gradient is proportional to the z^{-4}, and it is originated from field inhomogeneity. In simulation section, the force gradient will be illustrated using Finite Element Method software.

Optical binding force (figure 12(c)) is the force between the tip and the particle placed in the vicinity of it. This force can be approximated by the dipole image theory as illustrated before, but with different assumption. Without going into detailed analysis, the total force on the tip can be written as:

$$F_{t_z} \approx \frac{k}{2} Im\{\alpha_t\}|E_{0x}|^2\tilde{z} - \frac{3(\alpha_{rt_z}\alpha_{rp_z} + \alpha_{it_z}\alpha_{ip_z})|E_{0z}|^2}{4\pi\varepsilon_0\varepsilon_m z^4} \qquad 2.3.2.5$$

$\alpha_{ip}, \alpha_{rp}, \varepsilon_m$ are imaginary and real part of the polarizability of the particle, and the relative permittivity of the medium. Note that the second component is the one that contains the spectroscopic information and it has z^{-4} distance dependence.

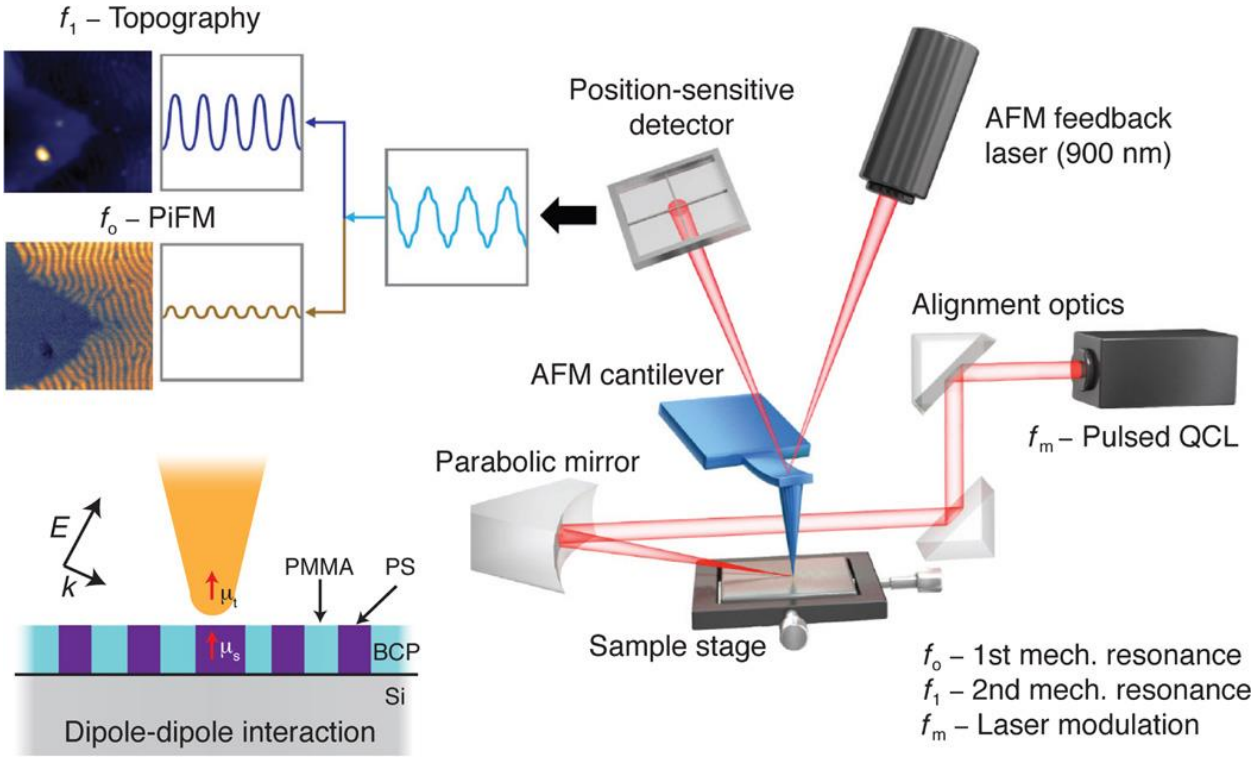

Figure 13: Basic layout of PiFM. adopted from [43]

In figure 13, PiFM employs the AFM cantilever tip with inverted optical microscopic structure. The light is received from two beams and focused into small spot to reduce the exposure of unexamined sample and to increase the intensity which magnifies the optical forces. The two beams are modulated at independent frequency. Typically, modulation frequency ranging from 100kHz to 10MHz. In this structure, the PiFM can measure the topography of the sample and the optical response at the same time. This can be achieved by driven the cantilever at f_{01} with certain amplitude. This frequency is responsible of the topographic image extracted from the sample. In this step, a control circuit will maintain

constant height by sensing the phase shift occurs on f_1 due to change in the optical forces between the tip and the sample. f_{01}can be any frequency i.e. first mechanical resonance. Because the cantilever exhibits multiple eigenfrequencies, one can utilize another resonance frequency $f_{02}$to detect the optical response. Figure 13 shows two images sample topography and PiFM image. f_{02}can be any frequency as long it is far from the first frequency f_{01}.

Demodulation the cantilever motions that corresponds to the optical modulation frequency allows detecting the photoinduced forces. The optical modulation frequency f_m can be f_1 if single beam is employed, or $f_1 \mp f_2$ if two-beam scheme is utilized. Depending on the aimed measurement PiFM can operate at two modes: direct-mode, where f_m is tuned to f_{02}, or sideband-mode, where $f_m \mp f_{01}$ is tuned to f_{02}. While sideband is good at extracting quantitative information, direct-mode allows more sensitive measurement to the gradient force.

2.3.3 Application:

The technique can be utilized to detect the linear and nonlinear optical properties of nanoparticle that display strong absorption features i.e. semiconductors in the visible range. PiFM has chemical imaging capabilities. An example is shown in figure 14 where there are two different polymers having different resonances at different wavelengths in the near IR range. By tuning the laser so that it covers both resonances for both polymers, optical contrast can be seen. The pictures in the figure are opposites revealing to resonances as illustrated in the figure. Another application related to mapping the electric field components of focused light, where the tip becomes a sensor of the near field, and

because the PiFM is capable of sensing the near field, it can be utilized to observe plasmon polaritons [62]. More promising application related to the subservice detection. An embedded nanoparticle in a sample can be detected using PiFM. It has been shown in the literature that by using sSNOM the nanoparticles embedded in the range of the tip radius can be detected with high spatial resolution. With PiFM, the resolution is expected to be higher because sSNOM technique relays on the scattering of the evanescent wave while PiPM measure the interaction forces directly.

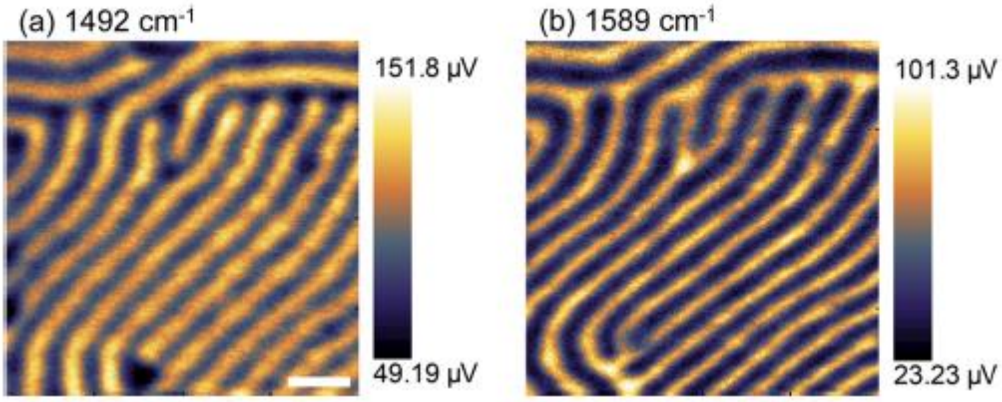

Figure 14: Chemical imaging for coblock polymer (PS-b-P2VP). The IR laser is incident at 1492cm-1 and 1589cm-1. (Adopted from [61])

Chapter3: COMSOL Simulation

3.1 Simulation Setup

Finite Element Method (FEM) with frequency domain approach has been utilized to analyze the tip-sample field components with three-dimensional mesh. A non-uniform meshing based on free tetrahedral elements is employed, where dense mesh elements are in the vicinity of tip-sample region with minimum element size of 0.1[nm]; the maximum size element is one tenth of the wavelength of the incident beam, which is required for converged solution. The dielectric constants of the set up are assumed to be uniform within the boundary of the tip, sample, and substrate. The set up will be modeled using 180^{o} mesh due to the symmetry in the configuration. The far-field boundary condition has been modeled using perfectly matched layer (PML). PML is very useful boundary condition for open boundary problems; it helps truncating the computational regions. It has been proven that PML is a strong absorbing layer which prevent waves impinging on it from reflecting back. The setup has been simulated using COMSOL Multiphysics software.

Optical forces that are sensed by the tip are strongly dependent on the absorption rate of materials, which is a frequency dependent phenomenon. The higher the absorption rate the higher the optical forces between tip and sample. Let assumed that a particle is adsorbed into a sample, where particle and sample have different absorption spectrum i.e. when the particle at resonance, the sample is transparent. If the particle is driven at resonance by incident monochromatic plane wave, the particle can be chased, and its location can be determined through observing force gradient curve which is affected by the particle location. The gradient rate is proportional to z^{-5} because gradient is derivative of force,

where z is the distance away from the tip. The particle location is swept from the surface of the PMMA until 200Å in depth (see figure 15).

To validate the theory, we have implemented the configuration shown in figure 15. The tip with 10^{o} half angle is terminated by sphere with radius of 100Å. The tip is, then, coated by gold with thickness of 50Å. Tip-sample distance is 5Å. PMMA with 300Å thickness is the host media of the Polystyrene (PS) particle; the PS particle radius is 50Å. The wavenumber of the monochromatic plane wave is set to be $700cm^{-1}$; at this wavenumber polystyrene has strong absorption peak while PMMA is transparent. The dielectric functions have been taken from [80] [81] [82]. The substrate is silicon and it is assumed to be infinite (it is not shown in figure 15). The sample has been irradiated by two monochromatic plane waves travelling in x-axis creating standing wave. The polarization of the electric field is in the z-axis i.e. parallel to the tip axis. The surrounding medium is air, and the far-field boundary condition is set to be perfectly matched layer (PML).

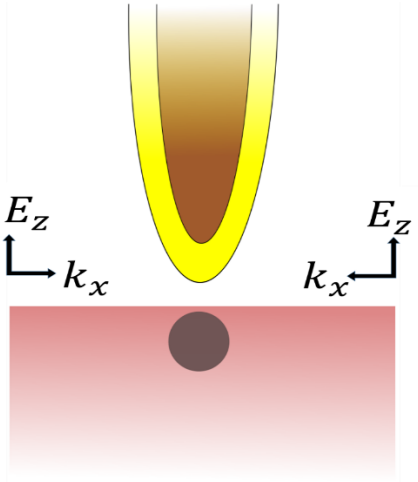

Figure 15: The configuration set up. Tip with 10^{o} half taper angle terminated by sphere of 100Å radius coated by gold with 50Å thickness. Tip-sample distance is 5Å. The geometry is irradiated by standing wave with polarization parallel to the tip axis. The PS particle is

embedded into PMMA sample, and swept into -z direction. In addition, The PS particle is scanned by sweeping the tip in x-axis. For both cases MST has been calculated.

3.2 Validating COMSOL Model and Equations

3.2.1 Closed Form Solution Validation: Mie Solution

Before starting to simulate a problem using Finite Element Method, the geometry of the problem must be validated. Validation can be done by solving a problem that is already solved by well-known publication and comparing the results of the simulation, or by implementing Mie analysis and compare the results to a well-known Mie solutions done by software code i.e. MATLAB. Mie theory describes the scattering and absorption process of an incident electromagnetic plane wave by a homogenous sphere. This case has been implemented (figure 16) to validate our geometry. In the figure, a sphere particle with radius of 1000Å and refractive index $n = 5 + 0.4i$ is irradiated by a monochromatic plane wave. The extinction cross section (ECS) has been analyzed and compared to analytical Mie solution done by Matzler code [83]. Due to symmetry, one quarter of the geometry is simulated to save computational time. COMSOL shows an excellent agreement with Mie solution (figure 16). Maxwell stress tensor (MST) is employed for force calculations. Therefore, validating MST equations used by COMSOL is inevitable. Irradiated particles are exposed to radiation force in the incidence direction. This force is proportional to the pressure cross section which is proportional to the extinction and scattering cross section. Once the pressure cross section is found, the radiation force can be calculated. Radiation force must equal the integration of MST over the particle surface. Figure 16 shows comparison between Mie solution and COMSOL results. MST equations results are identical

to the radiation force calculated by COMSOL and Matzler code. This enhances our confidence on COMSOL analysis.

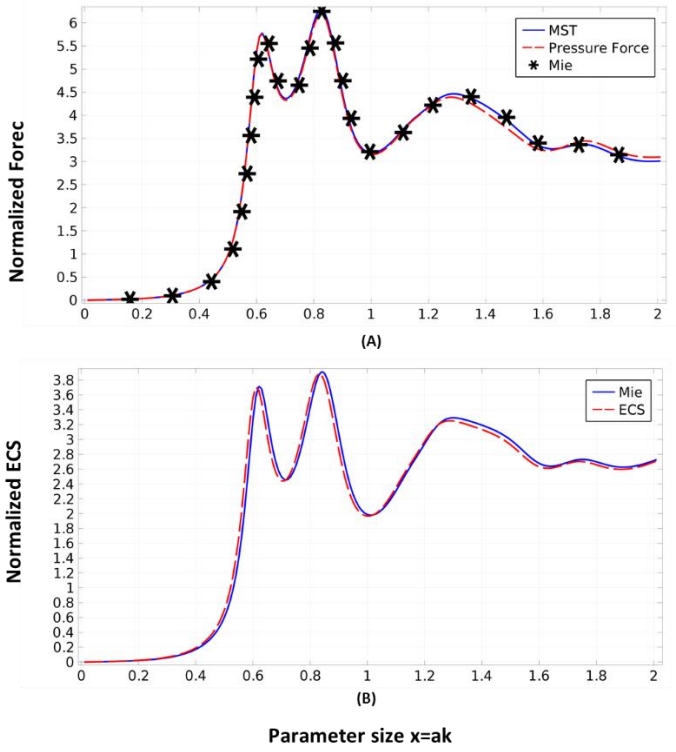

Figure 16: (A) shows comparison between MST and pressure force calculated by COMSOL i.e. COMSOL equations, and calculated using Mie analysis; y-axis is normalized. (B) Extinction cross section of a sphere with radius of a=100 [nm] irradiated by monochromatic plane wave; the dotted line and solid line are COMSOL results and the asterisk is Mie results. The x-axis is parameter size x=ak, where a is sphere radius and k is wave number.

3.2.2 Bench Mark:

To add more confidence to our geometry, the simulated configuration done by [84] is repeated (figure 17). In this configuration, solid silver tip is irradiated by monochromatic plane wave with wavelength of 632.8nm, where the incident angle is π/3. The tip is free

surrounded by air, and modeled as a solid metal cone terminated by sphere with radius of 250Å. Dielectric constants are the same as in [84]. The resulting field is normalized to the incident field. Therefore, the result shown in figure 17 is the field enhancement. The result is in good agreement with what is published in [84]. After validating our geometry using Mie analysis and previous published work problem, we are ready to simulate our configuration.

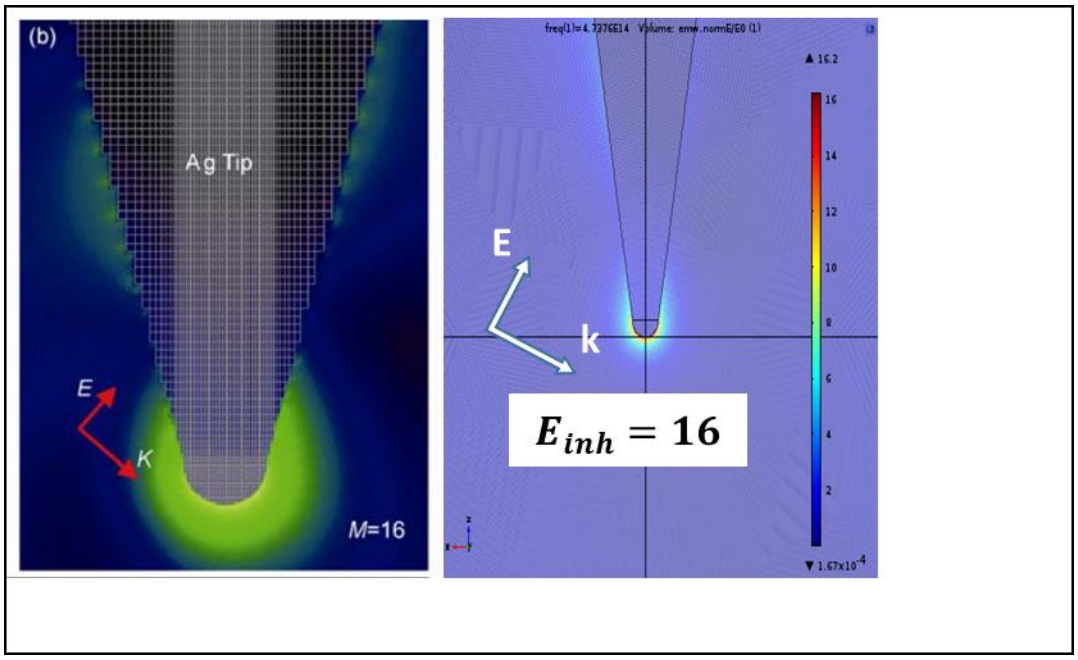

Figure 17: FDTD (left) [48] vs COMSOL (right) Ag solid tip illuminated by an incident field with pi/3 incident angle. The wavelength is 632.8nm $E_{inh} = \frac{E_{loc}}{E_{inc}}$*, where* E_{loc} *[V/m] is the electric filed at the tip, and* E_{inc} *[V/m] is the incident filed.*

3.3 Optimization:

In this section, we will study the effect of sample thickness and tip-coating thickness on the electric filed enhancement in the gap, and the field gradient in the sample to optimize the configuration. The effect of the Si substrate, which is not shown in figure 15, should be large to enhance the filed in the gap, which means higher force exerted on the tip.

Therefore, several PMMA thicknesses has been tested and the result shown in figure 18. It is obvious that Si substrate effect is eliminated at the thickness of 50nm, where the field enhancement is dominated by the PMMA only, and becomes thickness independent (saturate) as PMMA thickness exceed 50nm. Substrate effect can be understood by understanding the capacitance effect between the probe and the substrate, and to strengthen the capacitance effect the PMMA thickness should be decreased. Due to the fact that we are interested to embed a particle with radius of 50Å, we decide to set the thickness to 300Å; this thickness match the experimental set up done by [78]. Three metals coating has been studied: silver, platinum, and gold. Both shows same field enhancement. Gold metal is chosen for coating with 50Å coating thickness; the smaller the coating thicknesses the higher the enhancement. The smaller the radius of the coated tip the stronger the gradient in the gap. Strong gradient enhances the spatial resolution. To conclude, PMMA thickness is chosen to be 300Å, and the tip is coated by gold with 50Å thickness.

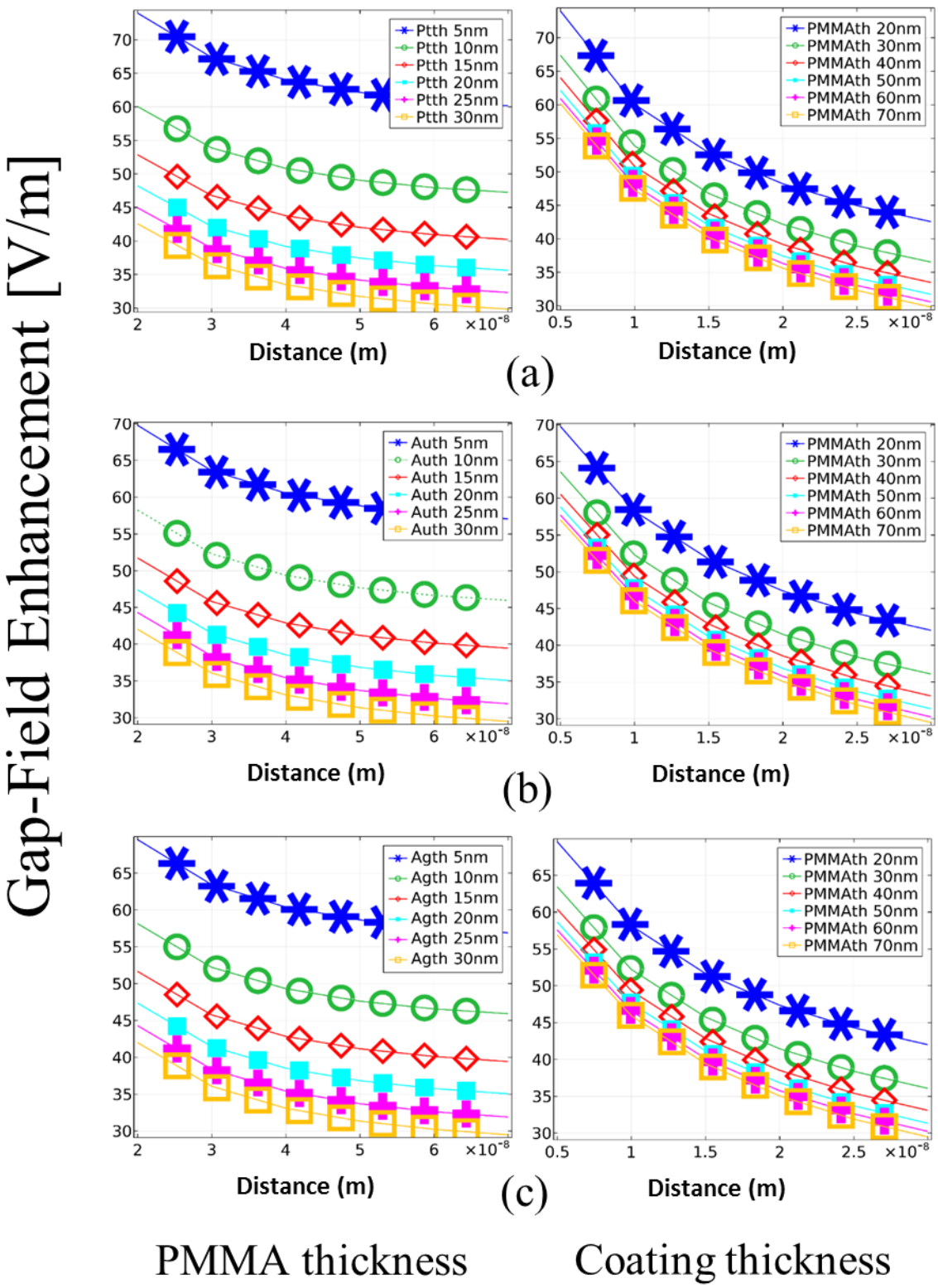

Figure 18: Gap-field enhancement as a function of PMMA thickness (left column) and coating thickness (right column). Row (a) tip has been coated by platinum, row (b) tip has been coated by gold, and (c) tip coating material is silver. Each curve is for fix coating thickness (left column) or fix PMMA thickness (right column). The incident wavelength is 10um.

3.4 Results

In this work, we are interested to observe the force sensed by the tip due to the presence of the PS particle which is driven at resonance by a standing wave $E(z) = E_0(e^{-ixk} + e^{ixk})\tilde{z}$ at 700 cm^{-1}, and embedded in PMMA layer. The tip-sample gap remains fixed while PS particle is swept in the -z direction i.e. away from the tip. Optical forces are function of the polarizabilities of the tip and sample.

MST has been integrated over the tip surface and force curve is shown in figure 19. As mentioned before, tip and sample can be assumed to be dipole and its image. If we assume that the dipole of the sample is dominated by the PS particle since it is driven at resonance, then the force exerted on the tip will be proportional to the PS particle location. The closer the particle to the tip the higher the force will be, and this is shown in figure 19. However, the force and PS particle location proportionality is not linear. The force is exponentially decreased, and it saturates once the PS particle location exceed a distance equal, roughly, the tip radius. The rapid decay in the force at short distance (close to the tip) is related to the rapid decay in the electrical field due to the inhomogeneity. Figure 16(A) illustrates the optical contrast. As the tip scan the sample and passes through the particle which is driven at resonance, the force shows lorenzian line shape. What matter is the difference between the maximum (tip above the particle) and minimum (tip away from the particle) force measured. Note that, for PS particle, at resonance, the deference is larger than when it is off resonance; this case cannot be generalized because ultimately this difference depends on the strength of the absorption index. For example, gold particle (figure 16(B)) is driven at resonance and off resonance, but in this case the off resonance wavelength is chosen to be

in the infrared region. The contrast is higher in the IR case than the resonance case, but the line width is larger, which indicates lower spatial resolution. The full width half maximum should not be the radius of the tip plus the radius of the particle because the effective field is confined into a smaller volume.

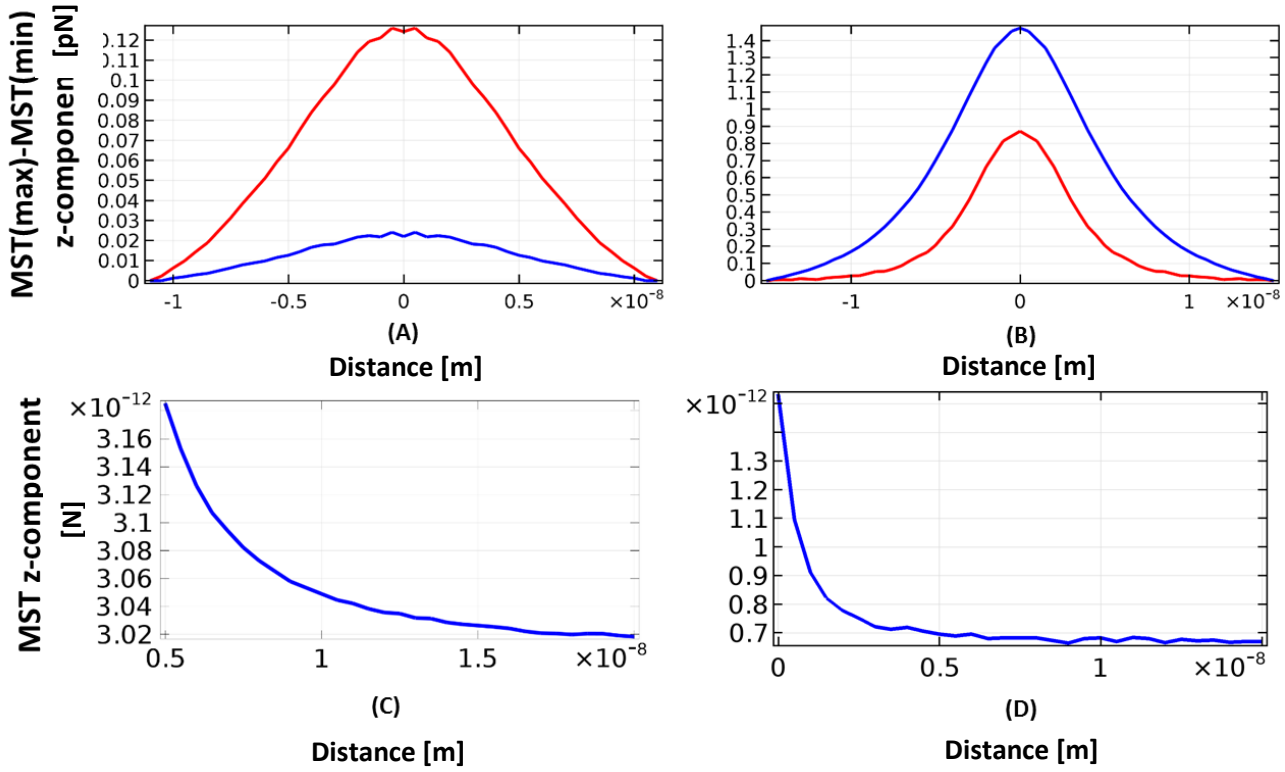

Figure 19: MST calculation on the tip due to the presence of the particle. (A) and (B) show the difference between the maximum MST (particle at the tip) and the minimum MST (particle away from the tip). For (A), red curve represents ON resonance case (n=1.9+0.12i and k=700cm-1) for PS particle and blue is OFF resonance (n= 1.65+0.005i and k= 625cm-1). For (B), red curve represents ON resonance case (n= 0.32+ 2.5789i and k=17543.86cm-1) for Au particle and blue is OFF resonance (n= 48.88+3346.2i and k= 625cm-1).

Subservice detection have been done by other techniques. For example, T. Taubner F.Keilmann and R. Hillenbrand [85] employ the sSNOM technique to detect embedded nanoparticles. They buried Au particles in Polymer layer with different thickness, and imaged the particles with best spatial resolution below 120nm. Relatively, this technique is

not suitable for imaging nanoparticles because the smaller the particle the less evanescent waves to be seen by the tip. In addition, the covering layer will significantly reduce the evanescent wave strength resulting in poor images. PiFM provides better spatial resolution well below 10nm. As illustrated in the figure 19 above, PS particle with radius of 5nm is resolved with different depth. While sSNOM is limited by far-field detection scheme, PiFM is limited only by the tip geometry, which means better signal to noise ratio, hence better imaging technique. Shekhawat, G. S., and V. P. Dravid demonstrate scanning technique that can be used to scan buried structure with high resolution, which they call scanning near-field ultrasonic holography SNFUH. Regardless to its high spatial resolution, the technique cannot be used to extract spectroscopic information since it detects perturbation caused by inhomogeneity in the sample [86]. Laurene Tetrad et al [87] utilized SNFUH to image nanoparticle in cells, but it shows structure of the particles but not the chemical properties. PiFM is a nondestructive technique that can be useful for studying toxicity of nanoparticle in cells; toxicity of nanoparticles depends on the physical and chemical properties of the nanoparticle [88] [89], and PiFM can detect spectroscopic properties and physical size of the nanoparticle. Therefore, it is an ideal technique for field of studying nanoparticles toxicity. Scanning depth of buried nanoparticles depends on the polarizability of the nanoparticle that is driven at resonance i.e. embedded metal, such as gold, nanoparticles scanning depth is deeper than soft nanoparticle scanning depth because metal has higher polarizability than soft material, such as PS. Applications of PiFM as scanning embedded nanoparticles can extend from material science to biological application. For example, if there is a particle buried in a sample, PiFM can predict particle compound by comparing the resulting force into known spectroscopic curve, where this can be done by tuning laser

frequency i.e. from optical regime into IR. PiFM can, in principle, be used to analyze nanoparticle populations in a host media i.e. biological cell. Nanoparticle coating due to interaction between the nanoparticle surface with the host media and purity analysis is a promising application for PiFM.

REFERENCE

[1] J. Z Young & F.Roperts, Nature, 167,231(1951).

[2] Wickramasinghe, H. K., Some History And Technology Of Scanning Microscopy. Scanning Microscopy Technologies and Applications., (1988).

[3] Binning G, Rohrer H, Gerber C, Weibel E, Phys. Rev. Lett., 49:52-61 (1982).

[4] Wickramasinghe, H. K., Scientific American, 261(4), 98-105, (1989).

[5] Eaton, P. J., & West, P. Atomic force microscopy (New York, 2010).

[6] Braga, P. C., & Ricci, D, Atomic force microscopy in biomedical research: Methods and protocols (New York: Humana Press, 2011).

[7] Jalili, N., & Laxminarayana, K., Mechatronics, 14(8), 907-945, (2004).

[8] Binnig, G., Gerber, C., Stoll, E., Albrecht, T., & Quate, C., Surface Science Letters, 189-190, (1987).

[9] Hansma, H. G., & Pietrasanta, L., Current Opinion in Chemical Biology, 2(5), 579-584, (1998).

[10] E.H. Synge: Philos. Mag. 6, 356 (1928)

[11] E.A. Ash, G. Nicholls: Nature 237, 510 (1972)

[12] A. Ruiter, J. Veerman, K. van der Werf, and N. van Hulst, Appl. Phys. Lett. 71, 28 (1997)

[13] B. Hecht, Forbidden Light Scanning Near-Field Optical Microscopy, Ph.D. thesis, University of Basel Hartung–Gorre, ISBN 3-89649-072-9, Konstanz, (1996).

[14] M. Pfeffer, P. Lambelet, and F. Marquis-Weible, Rev. Sci. Instrum. 68, 4478 (1997)

[15] B. Hecht, D. Pohl, H. Heinzelmann, and L. Novotny, in Ref. 40, Vol. 300, p. 93.

[16] R. Toledo-Crow, P. Yang, Y. Chen, and M. Vaez Iravani, Appl. Phys. Lett. 60, 2957 (1992)

[17] E. Betzig, P. Finn, and S. Weiner, Appl. Phys. Lett. 60, 2484 (1992)

[18] B. Hecht et al., J. Appl. Phys. 84, 5873 (1998)

[19] Bert Hecht et al, Journal of Chemical Physics, volume 112 No. 18, (2000)

[20] E. Betzig et al., Science 251, 1468 (1991)

[21] G. Valaskovic, M. Holton, and G. Morrison, Appl. Opt. 34, 1215 (1995)

[22] D. Turner, US Patent 4,469,554 (1984)

[23] P. Hoffmann, B. Dutoit, and R.-P. Salathe´, Ultramicroscopy 61, 165 (1995)

[24] P. Lambelet et al., Appl. Opt. 37, 7289 (1998)

[25] H. Heinzelmann, D. W. Pohl, Appl. Phys. A 59, 89-101 (1994)

[26] H. K. Wickramasinghe and C. C. Williams, “Apertureless near field optical microscope,” US Patent 4 947034, (1990)

[27] Hecht et al, J. Chem. Phys., Vol. 112, No. 18, (2000)

[29] Xie, X. S., Holtom, G. R., Mets, L., Dunn, R. C. Ultrafast Phenom. 9 (1994)

[28] Betzig, E., Chichester, R. J. Science, 262, 1422-1425, (1993)

[30] Xie, X. S., Dunn, R. C., Eds., World Scientific Publishing Co, (1996)

[31] Dunn, R. C., Holtom, G. H., Mets, L., Xie, X. S. J., Phys. Chem., 98, 3094-3098, (1994)

[32] van Hulst, N. F., Moers, M. H. P. IEEE Eng. Med. Biol., 51-57, (1996)

[33] Moers, M. H. P., Kalle, W. H. J., Ruiter, A. G. T., Wiegant, J. C. A. G., Raap, A. K., Greve, J., deGrooth, B. C., van Hulst, N. F. J. Microscopy, 182, 40-45, (1996)

[34] Iwabuchi, S.; Muramatsu, H.; Chiba, N.; Kinjo, Y.; Murakami, Y.; Sakaguchi, T.; Yokoyama, K.; Tamiya, E. Nucleic Acids Res., 25, 1662-1663, (1997)

[35] Robert C. Dunn, Chem. Rev., 99, 2891-2927, (1999)

[36] Jackson J. D., *Classical Electrodynamics*, Wiley Text Books, New York, (1998).

[37] Knoll B. and Keilmann F., Opt. Commun., 182-321, (2000)

[38] Zenhausern F., O'boyle M.P. and Wickramasinghe H. K., Appl. Phys. Lett., 65-1623 (1994).

[39] Fisher U. C., Heimel J., Maas H. J-. Hartig M., Hoeppener S. and Fuchs H., Surf. Interface Anal., 33-75 (2002)

[40] S. Patan`e et al, Rivista Del Nuovo Cimento, Vol. 27, N. 1, (2004)

[41] Achim Hartschuh et al., Physical Review Letters, Vol. 90 N. 9, (2003)

[42] Norikiko Hayazawa et al., The Journal of Chemical Physics, 117, 1296 (2002)

[43] Nowak et al. Sci. Adv. 2: e1501571, (2016)

[44] Lukas Novotny and Stephan J. Stranick, Annu. Rev. Phys. Chem., 57:303–31, (2006)

[45] Y. De Wilde and P. A. Lemoine, AIP Conference Proceedings 931, 43 (2007)

[46] Jalili, N., & Laxminarayana, K., 14(8), 907-945. (2004)

[47] Binnig, G., Gerber, C., Stoll, E., Albrecht, T., & Quate, C., Surface Science Letters, 189-190. (1987)

[48] Hansma, H. G., & Pietrasanta, L., Current Opinion in Chemical Biology, 2(5), 579-584. (1998)

[49] Braga, P. C., & Ricci, D. (2011). Atomic force microscopy in biomedical research: Methods and protocols. New York: Humana Press.

[50] Eaton, P. J., & West, P., Atomic force microscopy. (2010).

[51] Wickramasinghe, H. K., Some History And Technology Of Scanning Microscopy. Scanning Microscopy Technologies and Applications., (1988)

[52] Wickramasinghe, H. K., Scanned-Probe Microscopes, Sci Am Scientific American, 261(4), 98-105, (1989)

[53] Yang, Zhilin, Qianhong Li, Fangxiong Ruan, Zhipeng Li, Bin Ren, Hongxing Xu, and Zhongqun Tian., Chin. Sci. Bull. 2635-642. (2010)

[54] Tretinnikov, O. N., Journal of Applied Spectroscopy, 64-68, (2008)

[55] Zolotarev, V. M., B. Z. Volchek, and E. N. Vlasova., Optics and Spectroscopy, 101.5 716-23, (2006)

[56] M. N. Polyanskiy. "Refractive index database," http://refractiveindex.info.

[57] "Thomas Young Oration of the Physical Society." Nature 167.4238 (1951)

[58] Rajapaksa, I., K. Uenal, and H. Kumar Wickramasinghe., Appl. Phys. Lett., 97.7 (2010):

[59] Jahng, Junghoon, Faezeh Tork Ladani, Ryan M. Khan, and Eric O. Potma., Complex Light and Optical Forces X, (2016)

[60] Huang, Fei, Venkata Ananth Tamma, Zahra Mardy, Jonathan Burdett, and H. Kumar Wickramasinghe., Scientific Reports, 5-10610, (2015)

[61] Jahng, Junghoon, Dmitry A. Fishman, Sung Park, Derek B. Nowak, Will A. Morrison, H. Kumar Wickramasinghe, and Eric O. Potma., Accounts of Chemical Research, 48.10 2671-679, (2015)

[62] Jahng, Junghoon, Faezeh Tork Ladani, Ryan Muhammad Khan, Xiaowei Li, Eun Seong Lee, and Eric Olaf Potma. Opt. Lett., 40.21 5058, (2015)

[63] Martin, Y., Williams, C. C. & Wickramasinghe, H. K, *J. Appl. Phys.* **61**, 4723 (1987).

[64] Hecht, B. *et al.*, *J. Chem. Phys.* **112**, 7761 (2000).

[65] Zenhausern, F., Martin, Y. & Wickramasinghe, H. K., *Science* **269**, 1083 (1995).

[66] Schnell, M. *et al.*, *Nat. Photon*. **3**, 287–291 (2009).

[67] Veerman, J. A., Garcia-Parajo, M. F., Kuipers, L. & van Hulst. N. F., *J.Microsc.* **194**, 477–482 (1999).

[68] Bauer, T., Orlov, S., Peschel, U., Banzer, P. & Leuchs, G., *Nature Photon*. **8**, 23–27 (2014).

[69] Fleischer, M. *et al.*, *Appl. Phys. Lett.* **93**, 111114 (2008).

[70] Feber, B. le, Rotenberg, N., Beggs, D. M. & Kuipers, L., *Nature Photon*. **8**, 43–46 (2014).

[71] Kihm, H. W. *et al.*, *Nat. Commun.* **2**, 451 (2011).

[72] Burresi, M. *et al.*, *Science* **326**, 5952, 550-553 (2009).

[73] Rajapaksa, K. Uenal, and H. K. Wickramasinghe, Appl. Phy. Lett. 97 , 073121 (2010)

[74] Rajapaksa, I. & Wickramasinghe, H. K., *Appl. Phys. Lett.* **99**, 161103 (2011).

[75] Jahng, J. *et al.*, *Phys. Rev. B* **90**, 155417 (2014).

[76] Kohlgraf-Owens, D., Greusard, L., Sukhov, S., Wilde, D. Y. &Dogariu, A., Nanotechnology 25, 035203 (2014).

[77] Kohoutek, J. et al., Nano Lett. , 11, 3378–3382 (2011).

[78] Jahng, Junghoon, Dmitry A. Fishman, Sung Park, Derek B. Nowak, Will A. Morrison, H. Kumar Wickramasinghe, and Eric O. Potma. Acc. Chem. Res.48.10 (2015)

[79] Junghoon Jahng, Jordan Brocious, Dmitry A. Fishman, Fei Huang, Xiaowei Li, Venkata Ananth Tamma, H. Kumar Wickramasinghe, Eric Olaf Potma, Phys. Rev. B. (2014)

[80] Tretinnikov, O. N. J Appl Spectrosc Journal of Applied Spectroscopy 75.1 (2008)

[81] Zolotarev, V. M., B. Z. Volchek, and E. N. Vlasova. Opt. Spectrosc. 101.5 (2006)

[82] M. N. Polyanskiy. "Refractive index database," http://refractiveindex.info.

[83] Mätzler, C., IAP Research Report, No. 2002-11, (2002).

[84] Yang, Zhilin, Qianhong Li, Fangxiong Ruan, Zhipeng Li, Bin Ren, Hongxing Xu, and Zhongqun Tian, Chin. Sci. Bull. 55.24 (2010)

[85] Taubner, T., F. Keilmann, and R. Hillenbrand. *Opt. Express* 13.22 (2005)

[86] Shekhawat, G. S., and V. P. Dravid, Science 310.5745 (2005)

[87] Tetard, Laurene, Ali Passian, Katherine T. Venmar, Rachel M. Lynch, Brynn H. Voy, Gajendra Shekhawat, Vinayak P. Dravid, and Thomas Thundat, Nature Nanotech 3.8 (2008)

[88] Borm, P. et al a review carried out for ECETOC. Part. Fibre Toxicol. 3, 11 – 46 (2006).

[89] Xia, Nano Lett. 6, 1794–1807 (2006)